The mechanical anisotropy in a tissue promotes ordering in hexagonal cell packing

Kaoru Sugimura[1,2,*,‡] and Shuji Ishihara[3,4,*,‡]

SUMMARY

Many epithelial tissues pack cells into a honeycomb pattern to support their structural and functional integrity. Developmental changes in cell packing geometry have been shown to be regulated by both mechanical and biochemical interactions between cells; however, it is largely unknown how molecular and cellular dynamics and tissue mechanics are orchestrated to realize the correct and robust development of hexagonal cell packing. Here, by combining mechanical and genetic perturbations along with live imaging and Bayesian force inference, we investigate how mechanical forces regulate cellular dynamics to attain a hexagonal cell configuration in the *Drosophila* pupal wing. We show that tissue stress is oriented towards the proximal-distal axis by extrinsic forces acting on the wing. Cells respond to tissue stretching and orient cell contact surfaces with the stretching direction of the tissue, thereby stabilizing the balance between the intrinsic cell junction tension and the extrinsic force at the cell-population level. Consequently, under topological constraints of the two-dimensional epithelial sheet, mismatches in the orientation of hexagonal arrays are suppressed, allowing more rapid relaxation to the hexagonal cell pattern. Thus, our results identify the mechanism through which the mechanical anisotropy in a tissue promotes ordering in cell packing geometry.

KEY WORDS: Hexagonal cell packing, Tissue mechanics, Force inference, *Drosophila*

INTRODUCTION

Epithelial and epithelial-derived tissues often pack cells into a honeycomb pattern to realize proper functioning of tissues by supporting structural strength, promoting the correct formation of cell polarity, etc. (Thompson, 1917; Wootton, 1992; Raphael and Altschuler, 2003; Classen et al., 2005; Cooper et al., 2008; Ma et al., 2008). Cell geometry (e.g. the eventual fraction of hexagonal cells) is highly reproducible in each epithelial tissue and is regulated by forces acting along the plane of the adherens junction, such as tension, which shortens a cell contact surface, and pressure, which counteracts tension to maintain the size of a cell (Fig. 1A) (Graner and Sawada, 1993; Mofrad and Kamm, 2006; Farhadifar et al., 2007; Käfer et al., 2007; Lecuit and Lenne, 2007; Honda et al., 2008; Rauzi et al., 2008; Aigouy et al., 2010; Dahmann et al., 2011; Eaton and Jülicher, 2011; Lecuit et al., 2011; Kasza and Zallen, 2011; Bosveld et al., 2012; Sano et al., 2012). Theoretically, developmental changes in cell geometry have been described as the minimization of a potential energy, by which the balance of cell pressures and cell junction tensions is considered (Honda, 1983; Graner and Sawada, 1993; Farhadifar et al., 2007; Käfer et al., 2007; Aegerter-Wilmsen et al., 2010). The relaxation process towards a hexagonal cell configuration is often slowed down by the existence of local energy-minimum states that satisfy the force balance, which suppresses reconnection of cell contact surfaces to change nonhexagonal cells into hexagonal ones. At present, little is understood about how such disorder in cell geometry is resolved

and/or escaped to realize the correct and robust development of hexagonal cell packing. Identification of such a mechanism of cell packing could shed light on aspects of the physical basis of multicellular pattern formation.

The *Drosophila* pupal wing epithelium, which prominently increases the fraction of hexagonal cells during the course of its development, provides an excellent model system in which to study cell packing (Fig. 1B). In phase I [from ~15-24 hours after puparium formation (APF)] of wing development, cells undergo one or two rounds of cell division, and the initial, nearly isotropic morphology of the cells becomes elongated along the proximal-distal (PD) axis of the wing (Fig. 1C) (Fristrom and Fristrom, 1993; Classen et al., 2005; Aigouy et al., 2010). In phase II (from ~24-32 hours APF), the bias in the lengths of cell contact surfaces exhibits a moderate decrease. In addition, extensive cell rearrangement occurs, and the formation of new cell contact surfaces is biased towards the PD direction (Fig. 1D). Studies based on sophisticated image analyses have clarified the regulation of cell rearrangement by planar cell polarity (PCP) proteins (Strutt and Strutt, 2009), Rap1 GTPase (Knox and Brown, 2002) and tissue stretching along the PD axis by hinge constriction (Classen et al., 2005; Aigouy et al., 2010; O'Keefe et al., 2012). However, the mechanism by which tissue stretching directs cell rearrangement is yet to be clarified. Moreover, the link between directional cell rearrangement and hexagonal cell packing is missing. Answering these questions require space-time maps of force/stress with molecular and cellular quantifiers.

Various *in vivo* mechanical measurement methods have been developed. In particular, laser ablation of individual cell junctions is used as a tool to evaluate the tension acting on a cell contact surface. Such measurements have shed light on how cell shape and rearrangement are regulated by the activity and/or localization of force-generating molecular machinery within a cell (Hutson et al., 2003; Rauzi et al., 2008; Paluch and Heisenberg, 2009; Bosveld et al., 2012). A new complementary approach to such subcellular and invasive measurements is force inference from cell shape and

[1]Institute for Integrated Cell-Material Sciences (WPI-iCeMS), Kyoto University, Kyoto 606-8501, Japan. [2]RIKEN Brain Science Institute, Saitama 351-0198, Japan. [3]Graduate School of Arts and Sciences, University of Tokyo, Tokyo 153-8902, Japan. [4]PRESTO, JST, Saitama 332-0012, Japan.

*These authors contributed equally to this work
‡Authors for correspondence (ksugimura@icems.kyoto-u.ac.jp; shuji@complex.c.u-tokyo.ac.jp)
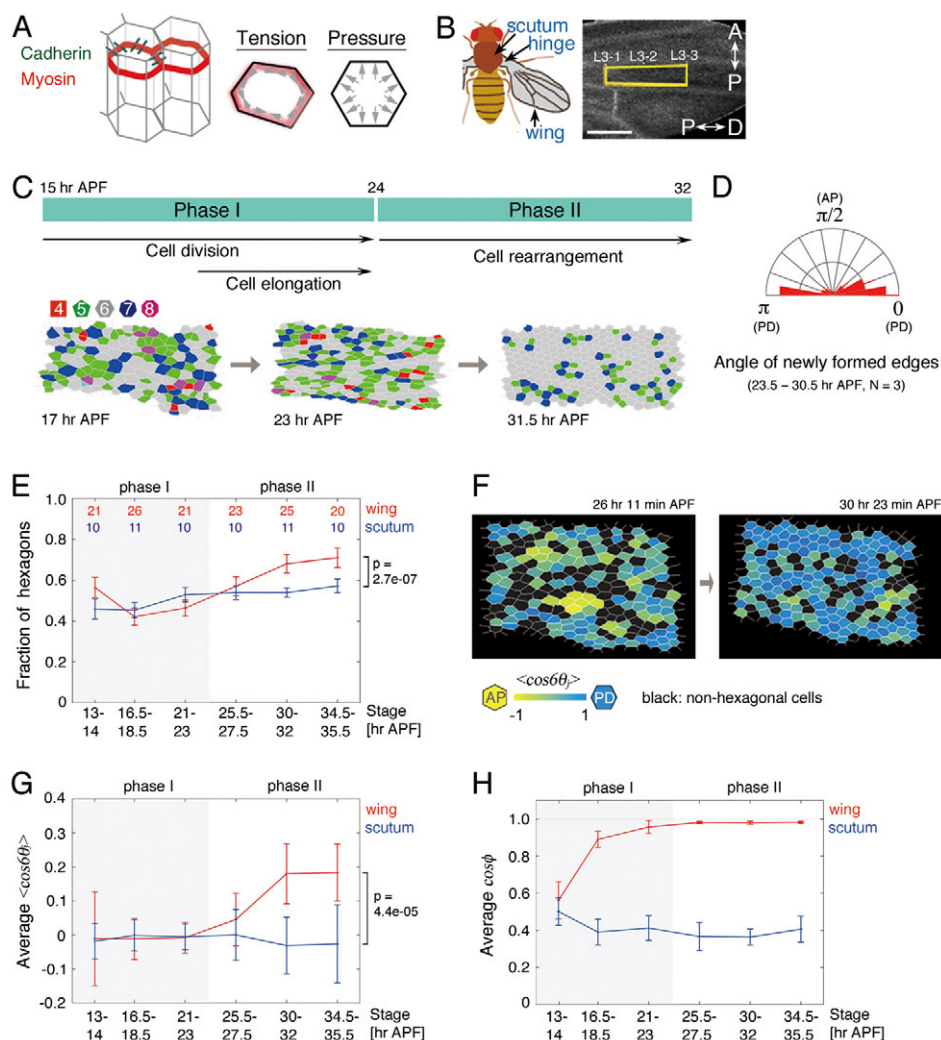
Fig. 1. Packing and alignment of hexagonal cells in the *Drosophila* pupal wing. (**A**) The structure and forces of an epithelial sheet. Cortical actin-myosin cables (red) run along the plane of the adherens junctions. Tension shortens a cell contact surface (an edge). Pressure maintains the size of a cell. (**B**) Left: Schematic of an adult *Drosophila*. Right: A wide image of the pupal wing at 32 hours APF. As spatial landmarks, we used three sensory organs on the L3 vein (L3-1 to L3-3) and analyzed the intervein region between L3-1 and L3-3 (rectangle). In all images of the pupal wing, the vertical and horizontal directions are aligned with the anterior-posterior (AP) and proximal-distal (PD) axes, respectively. We set a line connecting L3-1 and L3-3 as the PD axis. (**C**) Cell-level dynamics in the *Drosophila* pupal wing (Aigouy et al., 2010). Wing cells at each stage are colored according to their number of edges (red, square; green, pentagon; gray, hexagon; blue, heptagon; magenta, octagon). (**D**) The average angular distribution of the newly formed edges during time-lapse imaging from 23.5 to 30.5 hours APF was quantified at 30.5 hours APF (*n*=3). (**E**) Developmental changes in the fraction of hexagonal cells in the wing (red) and scutum (blue). Mean ± s.d. are plotted. The number of flies examined is indicated. (**F**) Hexagonal cells are color-coded by $\langle \cos 6\theta_j \rangle$ (the average of $\cos 6\theta_j$, where θ_{1-6} represents the angle of the edges belonging to the cell; supplementary material Fig. S1A). PD- and AP-oriented hexagons are colored blue and yellow, respectively. Nonhexagonal cells are shown in black. Time-lapse imaging was conducted from 23.5 to 30.5 hours APF. (**G,H**) The average values of $\langle \cos 6\theta_j \rangle$ (G) (supplementary material Fig. S1A) and $\cos \varphi$ (H) (supplementary material Fig. S1B) in each wing or scutum were calculated, and the mean ± s.d. among samples at each developmental stage is plotted. The number of control flies examined is the same as in E. The fly genotype was *sqhp-sqhGFP, apterous-gal4/sqhp-sqhGFP, UAS-Da-catenin-TagRFP*.

connectivity, which offers cellular resolution and is both global and noninvasive (Chiou et al., 2012; Ishihara and Sugimura, 2012). In our previous study, we formulated a Bayesian framework of force inference, in which all the cell junction tensions, differences in pressures among cells, and tissue stress are simultaneously inferred from the observed geometry of cells, up to a scaling factor (supplementary material Appendix S1). We have shown that inferred force and stress values are consistent with those obtained using other methods, such as laser ablation of cortical actin cables, quantification of myosin concentration and photo-elasticity (Nienhaus et al., 2009), and large-scale tissue ablation (Bonnet et al.,

2012; Ishihara and Sugimura, 2012; Ishihara et al., 2013). The global and noninvasive nature of the Bayesian force-inference method uniquely enables us to quantify space-time maps of force/stress in tissues and to relate the maps to hexagonal cell packing processes.

In this study, we address how forces and stress promote ordering of cell packing geometry in the *Drosophila* pupal wing. Force-inference analysis showed that tissue stress remained highly anisotropic until early phase II of wing development, when hexagonal cell packing occurred. We determined that anisotropic tissue stress promoted hexagonal cell packing by suppressing

mismatches in the orientation of hexagonal arrays. Furthermore, our results indicated that a PCP protein, Flamingo (Fmi; Starry night, Stan – FlyBase), was indispensable for hexagonal cell packing after the balance between the extrinsic and intrinsic forces was nearly stabilized.

MATERIALS AND METHODS

Drosophila strains
The flies used in this study were *sqhp-sqhGFP* (Royou et al., 2004), *DEcadherin-GFP* knock-in (Huang et al., 2009), *UAS-Dα-catenin-TagRFP* (Ishihara and Sugimura, 2012), *tubP-gal80^{ts}* (Bloomington Stock Center #7108), *UAS-sqh* dsRNA (Bloomington Stock Center #33892) and *UAS-flamingo* dsRNA (Shimada et al., 2006). Flies were raised at 25°C unless otherwise noted.

Immunohistochemistry
Anti-DCAD2 (Shg – FlyBase) (Oda et al., 1994) and anti-Zipper (kindly provided by Fumio Matsuzaki, RIKEN CDB, Japan) antibodies were used in this study. Pupae at appropriate ages were dissected, and wings were fixed at room temperature for 30 minutes in PBS containing 4% paraformaldehyde. After washing with PBS containing 0.1% Triton X-100, these preparations were incubated with the antibodies indicated above.

Image collection and analysis
Preparation of samples of the *Drosophila* pupal wing and scutum for image collection was conducted as previously described (Shimada et al., 2006; Koto et al., 2009; Ishihara and Sugimura, 2012). Images were acquired using an inverted confocal microscope (FV1000D; Olympus) equipped with an Olympus 60×/NA1.2 SPlanApo water-immersion objective at 25°C unless otherwise noted. An inverted confocal microscope (A1R; Nikon) equipped with a 60×/NA1.2 Plan Apochromat water-immersion objective was also used (Fig. 2; Fig. 3E; Fig. 4; Fig. 7C,D; supplementary material Fig. S9). After imaging, we confirmed that the pupae survived to at least the pharate stage. Images were processed and analyzed as previously described (Ishihara and Sugimura, 2012).

Laser ablation experiment
To measure the relative value of cell junction tension, laser ablation of the single contact surface was performed as described previously (Ishihara and Sugimura, 2012). The displacement of the vertices at 16 seconds after laser irradiation was used to calculate V_{max} of the vertices (the vertex displacement at 11 seconds was used in the previous study). To evaluate the anisotropy of global stress, a two-photon laser tuned to 720 nm wavelength (Chameleon; Coherent) was used to ablate a group of cells. Images were acquired using an inverted confocal microscope (SP5; Leica) equipped with a Leica 60×/NA1.2 HCX water-immersion objective. The displacement of cells at 14 seconds after laser irradiation was measured to calculate the difference between the velocity of cell groups along the PD and anterior-posterior (AP) axes ($V_x - V_y$).

Mechanical manipulation to relax tissue stretch
To test the possibility that anisotropic tissue stress plays an important role in hexagonal pattern formation, the wing was detached with the hinge by forceps at 23.5-24 hours APF, as previously described (Aigouy et al., 2010). We also employed a different method of relaxing tissue stretch: a two-photon laser tuned to 800 nm wavelength (Chamereon; Coherent) cut the wing along the anterior cross vein at 23.5-24 hours APF. A decrease in tension anisotropy was confirmed by laser cutting (data not shown). We adjusted the strength of laser irradiation to avoid damage to the wing. Only pupae that normally developed prehairs of wing cells were included in further analyses (100% of the samples cut by forceps and >60% of the samples cut by laser).

Statistics
Data are presented as mean ± s.d. *P*-values were calculated based on the Wilcoxon rank sum test. We characterized anisotropy in the inferred values for tension, the lengths of the cell contact surfaces, and the signal intensity of MRLC-GFP towards the PD axis using circular statistics (Fisher, 1993).

Force inference and numerical simulations
Detailed information on these methods is given in supplementary material Appendix S1.

RESULTS

The alignment of hexagonal cells proceeded over the same time course as the increase in hexagonal cells in the *Drosophila* wing

In the *Drosophila* pupal wing, the fraction of hexagons gradually decreased after cell division began (phase I; Fig. 1E). Then, the increase in hexagonal cells became prominent after the cells stopped dividing (phase II). We characterized developmental changes in hexagonal cell shape using the following quantities: (1) the orientation of hexagonal cells, which was defined by the average of $\cos 6\theta_j$, where θ_{1-6} are the edge angles ($\langle\cos 6\theta_j\rangle$; supplementary material Fig. S1A) and (2) the orientation of cell shape anisotropy, which was defined by the angle of the longest axis of a fitted ellipse ($\cos\varphi$; supplementary material Fig. S1B). We found that hexagonal cells increasingly pointed to the PD axis during phase II (more blue cells at later time points in Fig. 1F; Fig. 1G), whereas the orientation of cell shape anisotropy continued pointing to the PD axis from mid-phase I onwards (Fig. 1H). Thus, the PD alignment, but not the PD elongation of hexagonal cells, proceeded over the same time course during which the fraction of hexagonal cells increased in *Drosophila* wings. The mechanical process, which underlies the packing and alignment of hexagonal cells during phase II of *Drosophila* pupal development, is addressed below.

Tissue stress remained highly anisotropic until early phase II of wing development, when hexagonal cell packing occurred

We started by evaluating maps of cell junction tension and tissue stress in the wing at several developmental stages (supplementary material Figs S2-S6) and by analyzing temporal changes in tension/stress maps from time-lapse data in phase II (Fig. 2). Force-inference analysis showed that distribution of the inferred tension was biased at the beginning of phase II (24 hours APF). Indeed, cell contact surfaces with higher and lower tension values were primarily located along the PD and AP directions, respectively (in Fig. 2A, arrows and arrowheads, respectively; see supplementary material Fig. S5 for results of laser cutting of a single cell contact surface). The myosin regulatory light chain-green fluorescent protein (MRLC-GFP) signal was more enriched on the PD edges than on the AP edges [in Fig. 2A′, yellow and blue arrowheads, respectively; see supplementary material Fig. S2F for the enrichment of myosin heavy chain protein (Kiehart et al., 1989) on the PD edges]. Thus, all of our data indicated that cell junction tension was stronger on the PD edges at 24 hours APF (see supplementary material Fig. S2A-E for patterns of inferred tension and myosin at each stage of wing development). We characterized the anisotropies of inferred tension, edge length and myosin towards the PD axis in each wing, where larger *R*-values indicated larger anisotropy (see supplementary material Fig. S3A for the definition of *R*-values). The quantification of *R*-values from time-lapse data indicated that the anisotropies of the inferred tension, cell shape and myosin gradually decreased during phase II (Fig. 2D; see supplementary material Fig. S3B and Fig. S4 for the average of *R*-values at each stage of wing development and their statistical tests).

We next evaluated tissue stress and local cell stress tensors by integrating inferred tensions and pressures of individual cells (Fig. 2E; supplementary material Appendix S1) (Batchelor, 1970; Ishihara and Sugimura, 2012), where the maximum stress direction
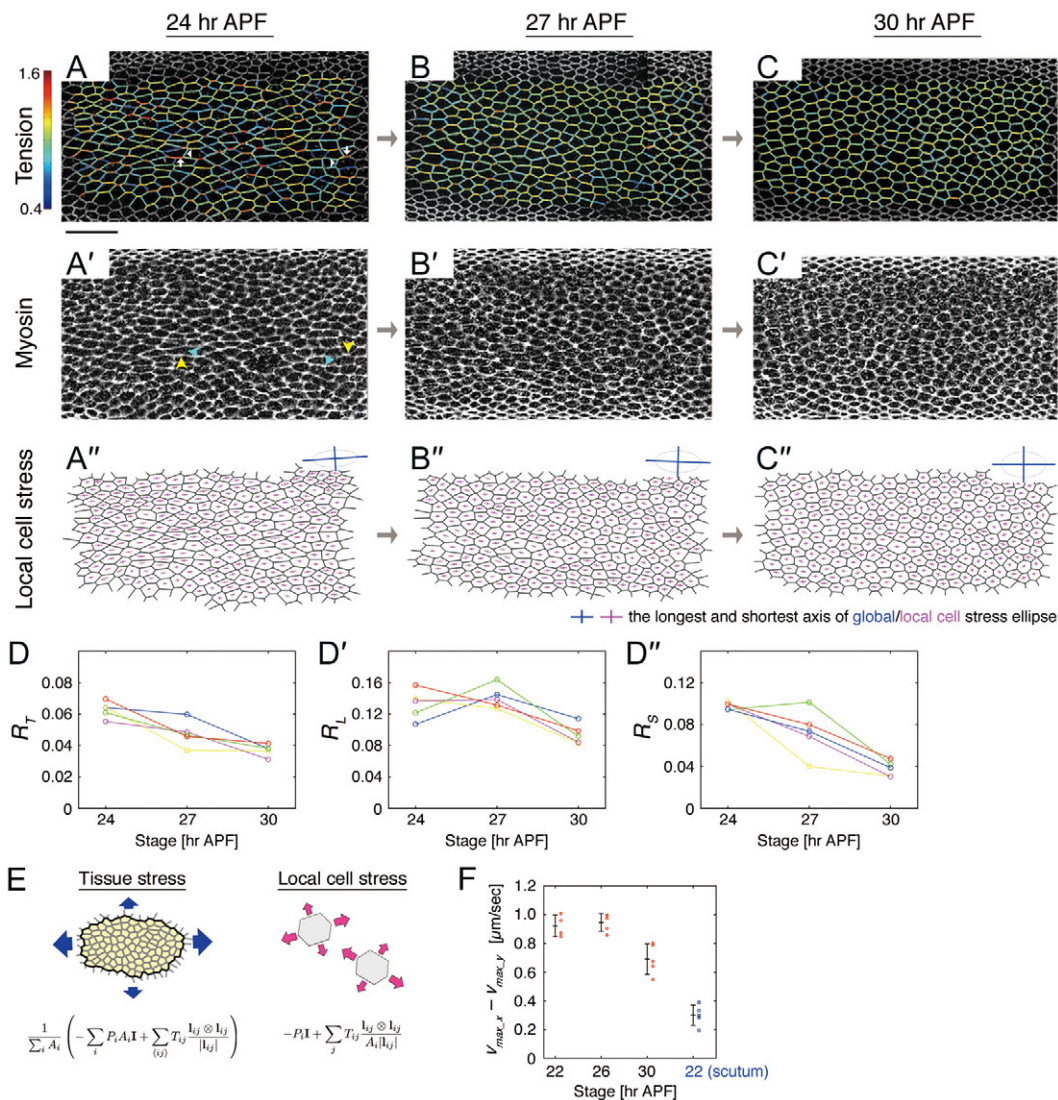
Fig. 2. Stress in the wing was stronger along the PD axis, when hexagonal cell packing occurred. (**A-C″**) Time-lapse analysis of the control wing from 24 to 30 hours APF (n=5). The inferred tension (A-C), MRLC-GFP (A′-C′), inferred local cell stress (A″-C″) and inferred tissue stress (insets in A″-C″; the longest axis of the stress ellipse represents the maximum stress direction) are shown. The PD and AP edges are indicated with arrows and arrowheads (A) and with yellow and blue arrowheads (A′), respectively. (**D-D″**) The anisotropy of the inferred tension (R_T; D), the length of the edge (R_L; D′) and the MRLC-GFP signal intensity (R_S; D″) are plotted (different colors represent different samples). (**E**) Schematics of global (tissue) stress and local cell stress (supplementary material Appendix S1) (Ishihara and Sugimura, 2012). The anisotropy of tissue stress was determined by geometrical and tension anisotropies (i.e. directional bias in the distribution of cell contact surfaces and that in tension values). This means that tissue stress can be anisotropic when tension is constant for all cell contact surfaces. (**F**) Tissue stress anisotropy was measured from global ablation data in the wing and scutum (supplementary material Movies 1, 2). The difference between the velocity of cell groups along the horizontal and vertical axes ($Vx - Vy$) was calculated from the displacement of cells at 14 seconds after laser irradiation, and the mean ± s.d. among samples at each developmental stage is plotted. Fly genotypes are *sqhp-sqhGFP*, *apterous-gal4/sqhp-sqhGFP*, *UAS-Da-catenin-TagRFP* (A-D) and *DECad-GFP* knock-in (F). Scale bar: 20 μm.

along which the stress was strongest in a cell/tissue was indicated by the longest axis of stress ellipses. Our force-inference analysis showed that the maximum stress direction of a cell/tissue pointed to the PD axis throughout phase II (Fig. 2A″-C″, magenta crosses, and blue crosses in insets, respectively). To examine experimentally tissue stress anisotropy, the group of cells shown in supplementary material Movie 1 was ablated, and the ablation contour was tracked; the anisotropic extension of the cell group contour confirmed the stronger tissue stress along the PD axis of the wing.

We next investigated whether tissue stress anisotropy decayed during phase II, as cell junction tension anisotropy did. The magnitude of the tissue stress anisotropy was quantified by

measuring the difference between the extension of the cell group contour along the PD and AP axes from large-scale tissue ablation data (e.g. supplementary material Movie 1) and by inferring the normal stress difference $\sigma_A \equiv (\sigma_{xx} - \sigma_{yy})/2$, which was used previously (Ishihara et al., 2013) to cross-validate the Bayesian force inference with large-scale tissue ablation (Bonnet et al., 2012). Both measurements indicated that tissue stress remained highly anisotropic until early phase II (~26-27 hours APF; Fig. 2F; supplementary material Fig. S6) when tension and myosin anisotropies had already started decreasing (Fig. 2A-D; supplementary material Fig. S2 and Fig. S3B).

Note that tissue stress anisotropy was determined by the directional bias both in the distribution of cell contact surfaces and in cell junction tension values (i.e. geometrical anisotropy and tension anisotropy, respectively; Fig. 2E). Accordingly, the discrepancy in the timing of the decrease of anisotropies of tissue stress and cell junction tension can be explained as follows: the decrease in tension anisotropy was compensated for by the increase in PD cell contact surfaces by cell rearrangement, thereby maintaining the anisotropy of tissue stress at high levels until early phase II, when hexagonal cell packing occurred.

## Anisotropic tissue stress was required and sufficient for promotion of hexagonal cell packing

Next, we examined the role of anisotropic tissue stress in promoting the formation of a hexagonal cell array. To highlight the importance of anisotropic tissue stress in controlling the polygonal distribution of cells, we compared cell geometry and force/stress maps of the wing with those of the scutum (anterior part of the dorsal thorax; Fig. 1B). We previously reported that tissue stress in the scutum is greater along the AP axis (supplementary material Fig. S3B-B″) (Ishihara and Sugimura, 2012); however, compared with the wing, the amplitude of the tissue stress anisotropy is weak (compare supplementary material Movies 1 and 2; Fig. 2F). The final fraction of hexagonal cells in the scutum was close to that in the wing at 13 hours APF when the tissue stress was isotropic (~60%; Fig. 1E), whereas the fraction of hexagons increased to >70% in the wing (Fig. 1E). In addition, the alignment of hexagonal cells to the tissue stretch axis was suppressed in the scutum (Fig. 1G). These observations suggested the possibility that strong anisotropic stress in tissue supported efficient hexagonal packing. Consistent with this hypothesis, a decrease in the number of
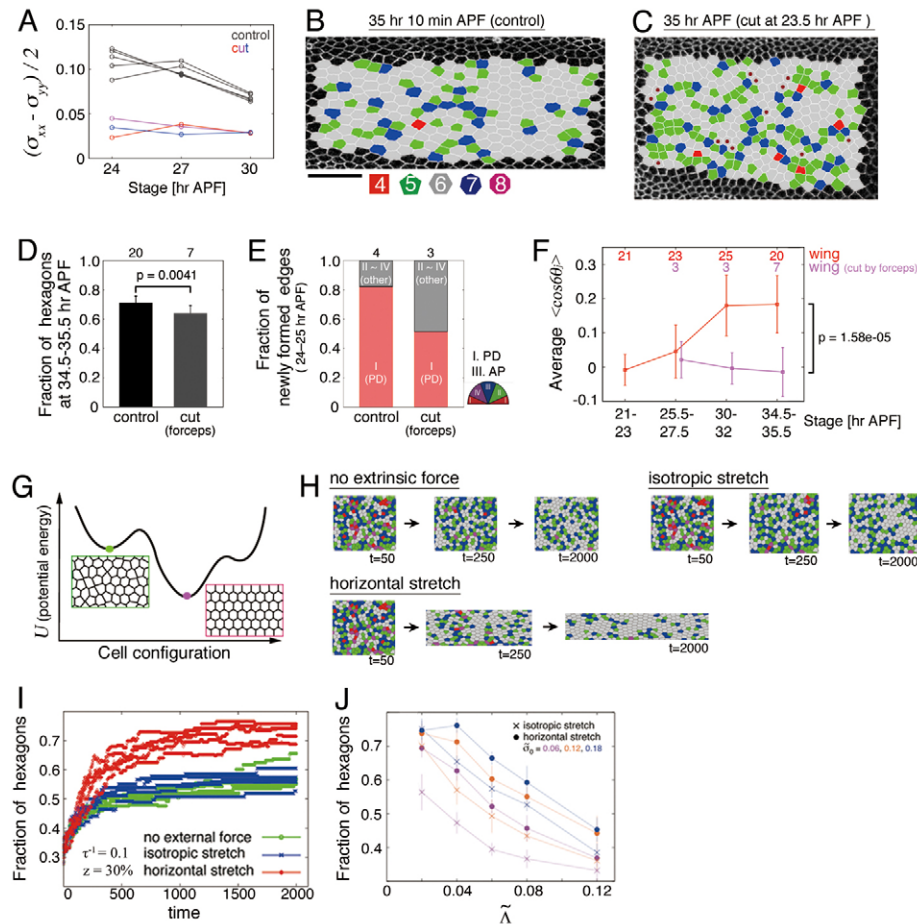
Fig. 3. Anisotropic tissue stress promoted hexagonal packing. (A) The inferred normal stress difference $\sigma_A \equiv (\sigma_{xx} - \sigma_{yy})/2$ is plotted for control wings and cut wings severed by forceps at 23.5-24 hours APF (different colors represent different samples). (B,C) Images of control (B) and cut (C) wings. Cells are colored according to the number of edges. The percentage of hexagonal cells was: 72.8% (B) and 59.6% (C). Circles in C label some of the AP-oriented cells. (D) Quantification of the fraction of hexagonal cells in control wings (as in B; left bar) and wings cut by forceps (as in C; right bar). (E) Quantification of cell rearrangement in the control and cut wings (n=4 and n=3, respectively). The angles of newly formed cell contact surfaces are measured from time-lapse data taken at 24-25 hours APF. The direction of each edge is classified as illustrated by the semicircle (e.g. red class I for the PD edges and blue class III for the AP edges). (F) The average value of $\langle \cos 6\theta_j \rangle$ in each wing or wing cut at 23.5-24 hours APF was calculated, and the mean ± s.d. among samples at each developmental stage is plotted. (G) Diagram of the relationship between potential energy and cell configuration. (H) Patterns of cells obtained by the numerical simulation of cell rearrangement without stretch, with isotropic stretch and with uniaxial (horizontal) stretch. t, time in numerical simulation steps. (I) Time evolution of the fraction of hexagonal cells in numerical simulation. The time scale and magnitude of noise are controlled by τ and z, respectively ($1/\tau$=0.1 and z=30%; see supplementary material Appendix S1, equations S2-S5). (J) Fractions of hexagonal cells at t=2000 in the numerical simulations are plotted for several values of $\tilde{\sigma}_0$ and $\tilde{\Lambda}$ ($1/\tau$=0.1 and z=30%; n=8 for each set of parameters). $\tilde{\sigma}_0$ and $\tilde{\Lambda}$ control the strength of the tension. The results of the simulations under isotropic stretch and horizontal stretch are indicated with crosses and circles, respectively. In D-F, the numbers of flies examined are indicated at the top. The fly genotype is as described in the legend of Fig. 1. Scale bar: 20 μm.
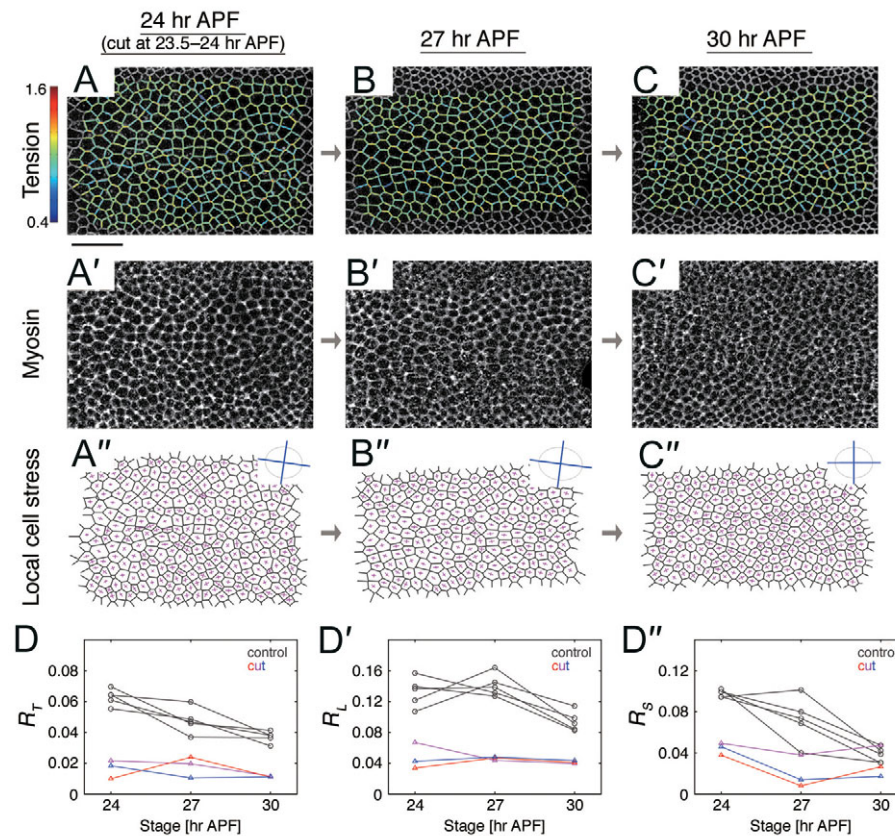
Fig. 4. The pattern of local cell stresses/cell junction tensions was dependent on anisotropic tissue stress. (**A-C″**) A pupal wing was detached from the hinge region by forceps at 23.5-24 hours APF and was observed at 24, 27 and 30 hours APF (n=3; the same set of samples was analyzed as in Fig. 3A). The inferred tension (A-C), MRLC-GFP (A′-C′), inferred local cell stress (A″-C″) and inferred tissue stress (insets in A″-C″; the longest axis of the stress ellipse represents the maximum stress direction) are shown. (**D-D″**) The anisotropy of the inferred tension (R_T; D), the length of the edge (R_L; D′) and the MRLC-GFP signal intensity (R_S; D″) are plotted (different colors represent different samples). Gray lines are the corresponding results for control wings (Fig. 2D-D″). Similar results were obtained by cutting a wing at 15 hours APF (n=11). The fly genotype was *sqhp-sqhGFP, apterous-gal4/sqhp-sqhGFP, UAS-Dα-catenin-TagRFP*. Scale bar: 20 μm.

hexagonal cells was observed by severing the wing from the hinge at an earlier developmental stage (Aigouy et al., 2010); however, further studies are necessary because pleiotropic effects, such as alternation of cell division patterns, are also induced by this technique (Aigouy et al., 2010; data not shown). We thus cut the wing at 23.5-24 hours APF to exclude effects on cell division. This mechanical manipulation significantly decreased the anisotropy of tissue stress (Fig. 3A) and resulted in a smaller fraction of hexagonal cells (Fig. 3B-D; supplementary material Fig. S7A-C). Moreover, the orientation of hexagonal cells was more disperse in the cut wings (Fig. 3C, circles label some of the AP-oriented cells), indicating that the orientation of hexagonal cells was improperly assigned (Fig. 3E,F; supplementary material Fig. S7D). Strongly anisotropic tissue stress was therefore required for the packing and alignment of hexagonal cells.

To determine whether anisotropic tissue stress was sufficient for promoting hexagonal packing, we performed numerical simulation of cell rearrangement under three conditions: no stretch, isotropic stretch and horizontal stretch (Fig. 3G-J; supplementary material Fig. S8; note that experimentally applying stretch to the pupal wing is technically very difficult). For numerical simulations, we modified the cell vertex model to control the anisotropic stress environment (supplementary material Appendix S1) (Honda, 1983; Graner and Sawada, 1993; Ouchi et al., 2003; Farhadifar et al., 2007; Käfer et al., 2007; Rauzi et al., 2008). Note that the hexagonal configuration was probably the energy-minimum state in each of the three conditions (Hales, 2001) (Fig. 3G), but local energy-minimum states hindered relaxation to the hexagonal state. Fluctuation could help the relaxation process by preventing a system from being trapped in a local minimum. We therefore introduced noise to the system by varying parameters in the line tension term

[in the wing, estimated tensions fluctuate about ±10% in 10 minutes (Sugimura et al., 2013)]. We found that unless the simulations were conducted under large noise with a slow time correlation, the eventual fraction of hexagonal cells under horizontal stretch was significantly larger than that under isotropic stretch (Fig. 3H-J; supplementary material Fig. S8B,C and Appendix S1 for results about dependence on noise parameters). These data indicated that horizontal stretch could drive an increase in hexagons, whereas the fluctuation in forces led to packing of cells into a hexagonal pattern in other conditions.

Cells rearranged cell contact surfaces to better align local cell stress and cell junction tension with global tissue stress

To understand the mechanism by which anisotropic tissue stress realized a rapid relaxation towards a hexagonal configuration, we addressed how cells responded to tissue stretch and changed cell packing geometry. For this, we manipulated extrinsic and intrinsic forces acting on the wing and monitored cellular responses to changes in the stress field in the tissue. Upon relaxation of tissue stress by detaching the wing from the hinge at 24 hours APF (Fig. 3A), cell shape anisotropy diminished, and cells decreased the degree of anisotropy of inferred tension, local cell stress, and myosin (compare Fig. 4A-D with Fig. 2A-D), indicating that the mechanical anisotropy of a cell was dependent on the tissue stretch. By contrast, when the cell junction tension was weakened by RNA interference (RNAi) against the *spaghetti squash* (*sqh*) gene, which encodes MRLC, excess shear deformation of cells was observed (supplementary material Fig. S9A,B). These results suggested that cells redistributed myosin and generated stronger intrinsic cell junction tension on the PD edges in order to resist tissue stretch that

was oriented towards the PD axis by extrinsic force (supplementary material Fig. S9C). This response of wing cells to balance the extrinsic force began in phase I, when the hinge constriction begins, because cutting the wing in phase I also diminished tension and myosin anisotropies (data not shown).

Next, we tracked force/stress and cell geometry from time-lapse data in phase II, when hexagonal cell packing proceeds, and examined how cells alter their force/stress and geometry to achieve balance against tissue stretch. Specifically, we evaluated the alignment and magnitude of cell junction tension/local cell stress with respect to tissue stress before and after the cell rearrangement/alignment process, keeping in mind that tissue stress was oriented towards the PD axis by extrinsic force (Fig. 5A). Force-inference analysis showed that the stress of individual cells deviated significantly at ~24 hours APF; some cells developed strongly anisotropic stress, whereas stress of others was almost isotropic (Fig. 5B). As hexagonal cells are pointing to the PD axis (Fig. 5C, horizontal axis), local cell stress exhibited similar anisotropy and magnitude along the direction of maximum global stress (Fig. 5B-E; supplementary material Fig. S10A,B). Over the same time course, the magnitude of inferred tension became

uniform (Fig. 5F), which possibly resulted from the fact that the increase of PD cell contact surfaces through cell rearrangement led to the decrease of mechanical load on each PD cell contact surface. These results showed that cells responded to anisotropic tissue stretch by orienting cell contact surfaces to align local cell stress/cell junction tension with the stretching direction of the tissue, thereby stabilizing the balance of intrinsic and extrinsic forces at the cell-population level (supplementary material Fig. S10C). Thus, global force balance assigned the orientation of wing cells, which concomitantly proceeded with hexagonal cell packing in the wing.

Comparison of extrinsic tissue stretch-driven mechanisms of cell rearrangement and intrinsic cell junction tension-driven mechanisms for promoting hexagonal cell packing
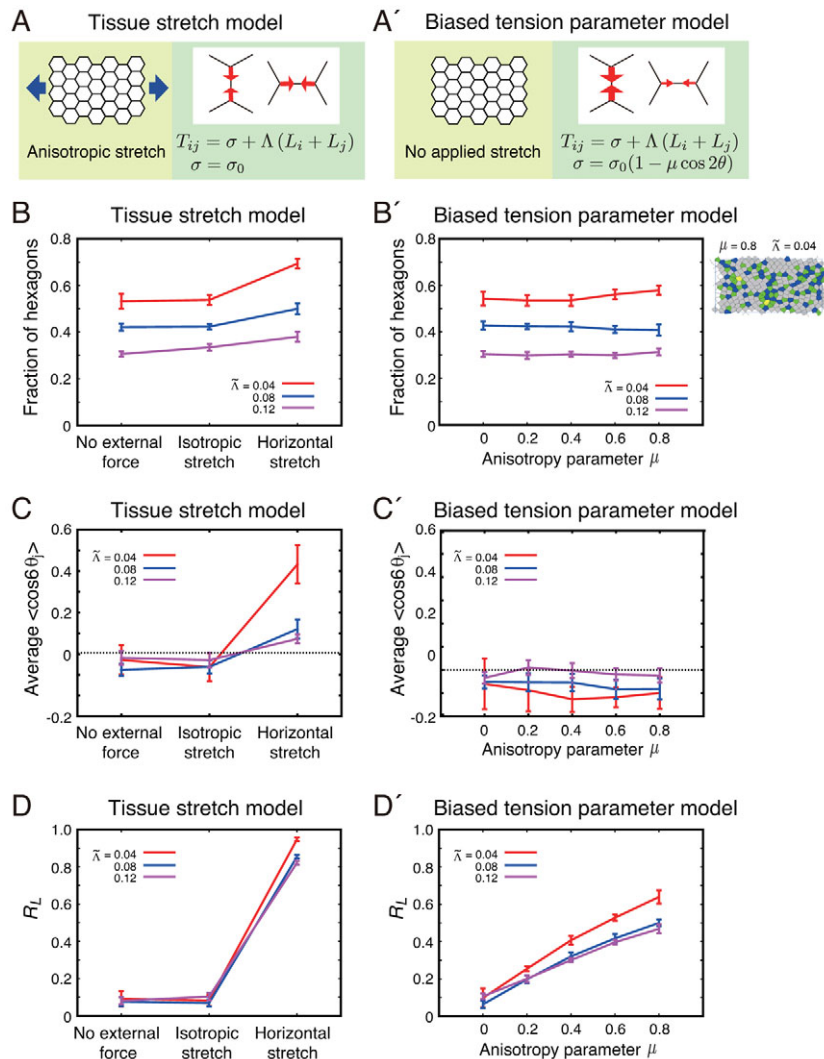
To support further the role of anisotropic tissue stress in controlling cell packing geometry, we numerically compared the mechanisms of cell rearrangement driven by extrinsic tissue stretch with those driven by intrinsic cell junction tension (Kasza and Zallen, 2011; Lecuit et al., 2011) for promoting hexagonal cell packing. For this, we performed two numerical simulations: (1) assuming that applied
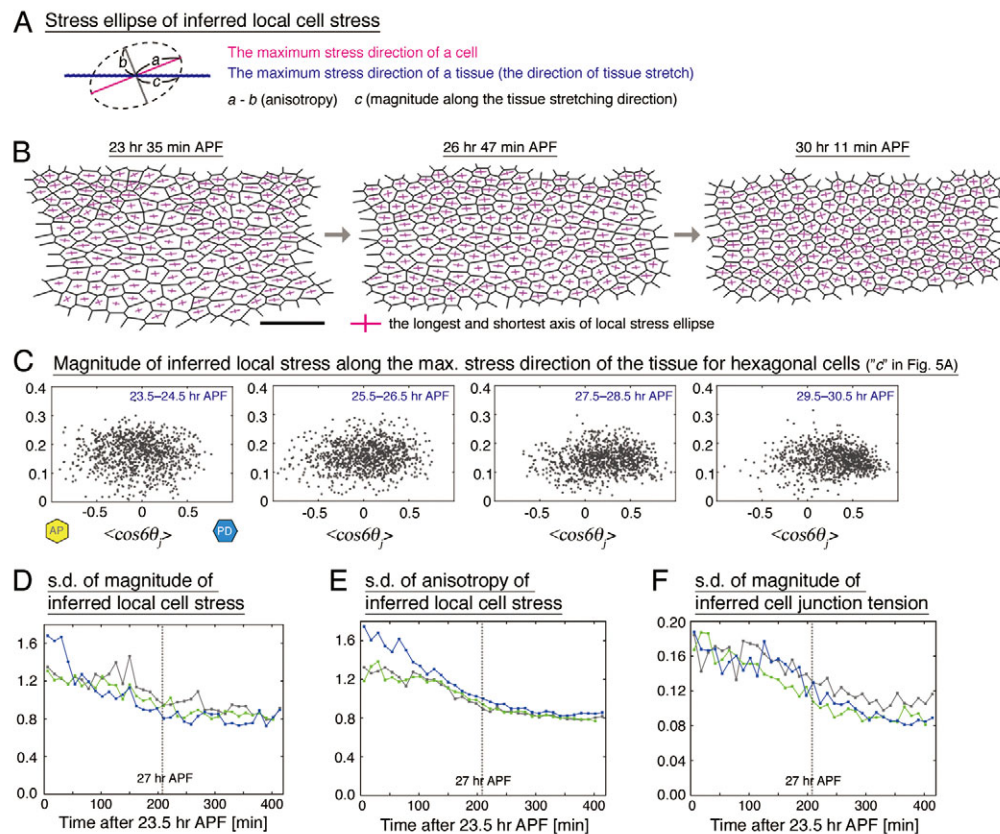
Fig. 5. The alignment of local cell stresses/cell junction tensions with global tissue stress during hexagonal cell packing. (A) The anisotropy of local cell stress and its magnitude along the maximum stress direction of the tissue were calculated by $a - b$ and c for each cell, respectively. (B-F) Developmental changes in inferred patterns of local cell stress and cell junction tension. Time-lapse data obtained from 23.5 to 30.5 hours APF were extracted at 12-minute intervals. (B) Images showing local stress of each cell, in which the crossed lines are the longest and shortest axes of the local stress ellipse of each cell. Initially, some cells exerted strong local stress along the PD axis, whereas others generated relatively weak and/or isotropic local stress. Then, the variance of local cell stress decreased, and individual cells eventually generated forces with similar anisotropy and magnitude along the maximum stress direction of the cell population (i.e. the PD direction). (C) The magnitude of local cell stress along the maximum stress direction of the tissue (c in A) for each hexagonal cell is plotted against its $\langle \cos 6\theta_j \rangle$. (D-F) Temporal changes in the standard deviation of the magnitude of local cell stress along the maximum stress direction of the tissue (D); in the standard deviation of the anisotropy of the local stress (E) ($a - b$ in A); and in the standard deviation of inferred tension are plotted (different colors represent different samples). The fly genotype was *sqhp-sqhGFP*, *apterous-gal4/sqhp-sqhGFP*, *UAS-Da-catenin-TagRFP*. Scale bar: 20 μm.

Fig. 6. Comparison between two mechanisms of cell rearrangement in hexagonal cell packing by numerical simulation. (**A**,**A'**) Numerical simulation of cell rearrangements. (A) Tissue stretch model. Isotropic or anisotropic tissue stretch by external forces was applied (as was performed in Fig. 3H). There was no angular bias in tension parameters. (A') No external force was applied. σ, a parameter to control the strength of tension, depended on the angle of cell contact surface, where the magnitude of the angular bias was controlled by μ. Here, vertical cell contact surfaces were set to generate larger tension than horizontal ones. Details of these numerical simulations are described in supplementary material Appendix S1. (**B**,**B'**) Fractions of hexagonal cells at t=2000 according to numerical simulations of the tissue stretch model (B; see also Fig. 3I) and the biased tension parameter model (B'). The eventual cell configuration is shown in the right panel for μ=0.8 and $\tilde{\Lambda}$=0.04. (**C**,**C'**) The mean ± s.d. of $\langle\cos6\theta_j\rangle$ among samples at each condition is plotted for the tissue stretch model (C) and the biased tension parameter model (C'). (**D**,**D'**) The anisotropy of the length of the edge (R_L) is plotted for the tissue stretch model (D) and the biased tension parameter model (D'). n=10 for each condition (B-D).

stretch was anisotropic, with no angular bias in parameters of cell junction tension (Fig. 6A; as was performed in Fig. 3H), and (2) vice versa (Fig. 6A'; supplementary material Appendix S1). Other parameters were the same in both numerical simulations. As mentioned before, the fraction of hexagonal cells increased in response to horizontal stretch (Fig. 6B; Fig. 3I). By contrast, fewer hexagonal cells were found in the biased tension parameter model (Fig. 6B'). The average of $\langle\cos6\theta_j\rangle$ increased by horizontal stretch (Fig. 6C), as was observed in the wing (Fig. 1G), but not in the biased tension parameter model (Fig. 6C'). Cells were relatively elongated along the horizontal direction in both the anisotropic tissue stretch model and the biased tension parameter model (Fig. 6D,D'). However, the angular dependence of tension was opposite between them; horizontal cell contact surfaces had larger tension than did vertical cell contact surfaces owing to the extrinsic tissue stretch in the former (intrinsic tension parameters were the same for all edges). By contrast, by definition of the model, horizontal cell contact surfaces had lower tension in the latter. These results indicated that numerical simulation with anisotropic tissue stretch agreed better with the experimental observations in terms of cell geometry and force.

In the wing, time-lapse data of cell rearrangement indicated that the inferred tension of shrinking AP edges was not as large as that of newly formed PD edges (Fig. 7A,B; supplementary material
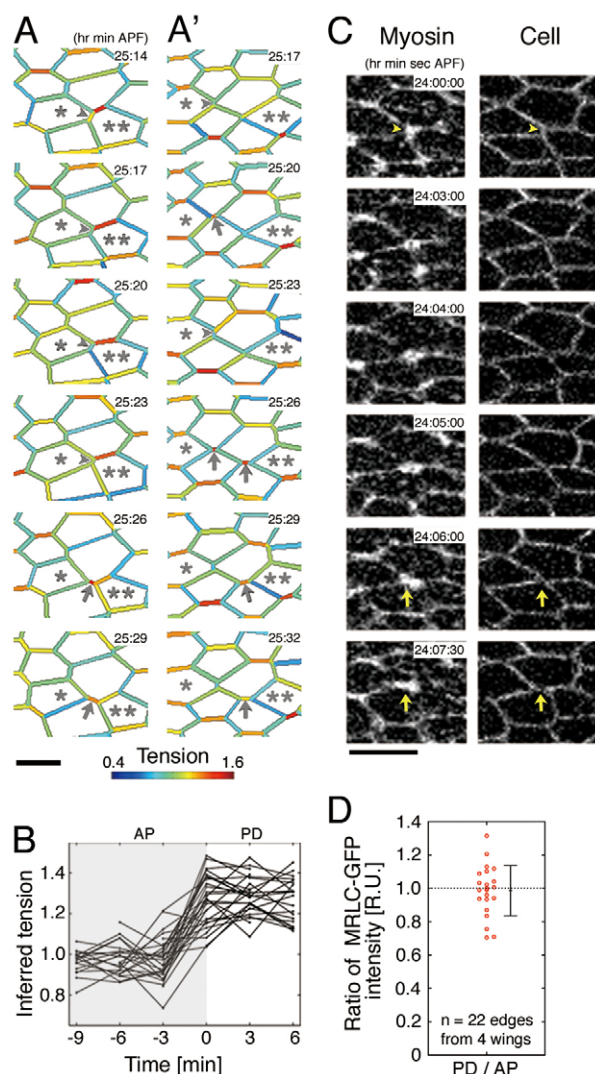
Movie 3). The level of MRLC-GFP signal intensity remained almost constant in newly formed PD edges [Fig. 7C,D; the ratio of MRLC-GFP signal intensity between shrinking AP edges and newly formed PD edges was 0.99±0.15 (n=22)]. Moreover, *sqh* RNAi in wing cells did not affect the PD bias in cell rearrangement [86% of the newly formed edges belonged to class I (see Fig. 3E for the classification of edges) (n=3); supplementary material Fig. S9 legend]. These results implied that intrinsic cell junction tension of shrinking AP edges did not primarily determine the direction of cell rearrangement in the wing. Taken together, both our computational and our experimental data further supported the role of anisotropic tissue stress in promoting hexagonal cell packing through rearrangement and alignment of cells.

A physical mechanism of hexagonal cell packing

To connect the mechanical force balance with cell packing geometry, we sought to determine how the orientation of hexagonal cells, which we showed was assigned by the mechanical force balance in the wing, led to efficient hexagonal cell packing. Our analysis of cell configurations clarified two characteristics of wing cells: (1) a spatial map of $\langle\cos6\theta_j\rangle$ indicated that hexagonal cells re-oriented to match their neighbors' orientation better (hexagonal array; Fig. 8A,B), and (2) nonhexagonal cells appeared at the boundaries of hexagonal arrays

Fig. 7. Dynamics of inferred tension and myosin during the PD intercalation of cells. (**A-B**) Tension of the cells was inferred from the time-lapse data from 23.5 to 30.5 hours APF. (A,A′) Patterns of the inferred tension. Asterisks indicate the corresponding cells in each frame. Arrowheads and arrows point to the AP and PD edges, respectively. (B) Temporal changes in the inferred tension of the shrinking AP edge and the newly formed PD edges in the wing shown in supplementary material Movie 3. The PD intercalation of cells occurred between −3 and 0 minutes. When an edge underwent multiple rounds of remodeling, data were divided into single series of the PD intercalation. (**C,D**) MRLC-GFP during junctional remodeling was tracked from the time-lapse data from 24 to 25 hours APF. (C) Time-lapse images of MRLC-GFP (left) and Dα-catenin-TagRFP (right). Arrowheads and arrows point to the AP and PD edges, respectively. (D) The ratio of the MRLC-GFP signal intensity between shrinking AP edges and newly formed PD edges. The MRLC-GFP signal intensity at 1.5, 1 and 0.5 minutes before PD cell rearrangement was measured and its average at the three time-points was calculated. The average of MRLC-GFP signal intensity at 0, 0.5 and 1 minute after PD cell rearrangement was calculated, and was divided by the value before junctional exchange. The fly genotype was *sqhp-sqhGFP*, *apterous-gal4/sqhp-sqhGFP*, *UAS-Dα-catenin-TagRFP*. Scale bars: 5 μm.

that point to different orientations (i.e. segregation of the hexagonal array; Fig. 8A). We characterized segregation of the hexagonal array by quantifying the difference between the largest and smallest $\langle \cos 6\theta_j \rangle$ among adjacent cells (denoted as D_i;

cumulative distributions are plotted in Fig. 8C). In Fig. 8C, the rightward shift of the blue lines at later developmental stages indicated that nonhexagonal cells present between the mismatched hexagonal cell arrays were more predominant after the cells were rearranged during hexagonal cell packing.

Based on these results, we propose a physical mechanism of hexagonal cell packing. In an isotropic stress field, local relaxation to hexagonal cells often causes a mismatch in the orientation of hexagonal arrays (e.g. white arrows in Fig. 9A point to different orientations in top and bottom hexagonal arrays); thus, nonhexagonal cells appear at the boundaries of the arrays because of topological constraints. By contrast, anisotropic tissue stress suppresses mismatches in the orientation of hexagonal arrays by endowing the cells with an inherent orientation (Fig. 9B). This accounts for a mechanism that allows for more rapid relaxation to the hexagonal cell pattern.

Flamingo (Fmi) was required for hexagonal cell packing when the global force balance was nearly stabilized

Finally, we studied the respective timings of actions of genetic and mechanical regulation in hexagonal cell packing. Among the PCP mutants examined, the flamingo (*fmi*) (Usui et al., 1999) mutant clone exhibited a relatively strong defect in hexagonalization (Classen et al., 2005) (see supplementary material Fig. S11A and its legend for evidence that that *fmi* RNAi did not significantly change mechanical parameters of the wing). Supplementary material Fig. S11B shows that the number of hexagonal cells increased in *fmi* RNAi wings, as was also observed in control wings, until 27.5 hours APF. After that, the increase and alignment of hexagonal cells was disrupted in *fmi* RNAi wings (supplementary material Fig. S11B,C, asterisks). Interestingly, anisotropic tissue stress began to weaken after 27 hours APF (Fig. 3A), and the alignment of local cellular forces to tissue stress was mostly completed around 27 hours APF (Fig. 5D-F). These results suggested that both of these forces and Fmi regulated hexagonal packing through the PD alignment of hexagonal cells, but that Fmi was indispensable for the process when the balance between the extrinsic and intrinsic forces was nearly stabilized (summarized in supplementary material Fig. S12A).

DISCUSSION

The present study aimed at unveiling the physical basis of tissue integrity via hexagonal cell packing. For this purpose, we utilized the Bayesian force-inference method to take a data-driven approach, in which the interplay between global stress in a tissue and local forces and shape changes of cells was analyzed. We determined that tissue stress remained highly anisotropic until early phase II of wing development when hexagonal cell packing occurred and that the mechanical anisotropy in a tissue promoted ordering of cell packing geometry (Fig. 9).

In the *Drosophila* wing, hexagonal cell packing is primarily achieved by cell rearrangement (Classen et al., 2005). Previous studies in other model systems, using subcellular and invasive force measurements, such as laser ablation of individual cell junctions, showed that the nonuniform localization of force-generating molecular machinery generates the angular bias in intrinsic cell junction tension, which triggers directional cellular rearrangements underlying tissue morphogenesis (supplementary material Fig. S12B, arrows 1 and 2) (e.g. Rauzi et al., 2008; Bosveld et al., 2012). By mapping forces inside the tissue, the present study highlighted a pivotal role of another physical ingredient, namely tissue stress, in
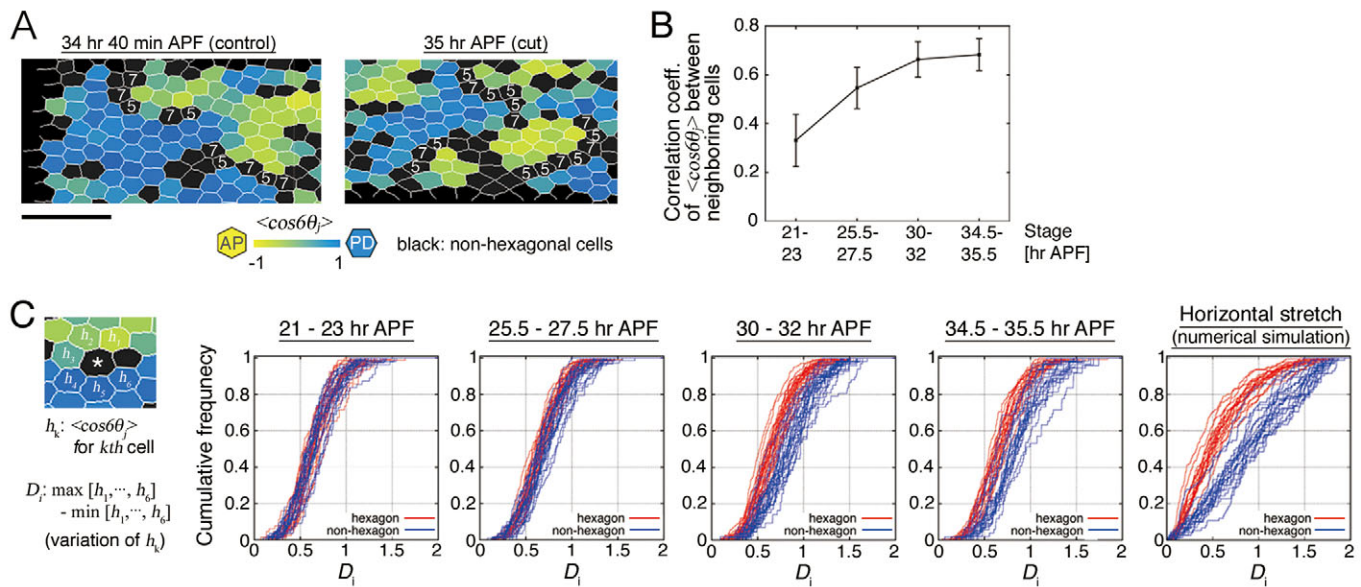
Fig. 8. Changes in the configuration of cells during hexagonal cell packing. (**A**) Images of control and cut (as in supplementary material Fig. S7) wings. Each hexagonal cell is colored according to $\langle\cos6\theta_j\rangle$. Nonhexagonal cells are shown in black. (**B,C**) Quantitative analysis of the segregation of hexagonal cell arrays. For clarity, h_i denotes $\langle\cos6\theta_j\rangle$ of the ith cell. (B) Developmental changes in correlation coefficients of h_i (i.e. $\langle\cos6\theta_j\rangle$) between neighboring hexagonal cells. The correlation coefficients were computed by $C = \sum_{[ij]}(h_ih_j - \bar{h}^2)/N_{HH}\bar{h}^2$, where $\sum_{[ij]}$ indicates taking the sum over adjacent pairs of hexagonal cells, and N_{HH} is the number of the pairs. The correlation coefficient increased up to ~0.7, indicating local alignment of hexagonal cell orientation (i.e. formation of a hexagonal cell array). The number of control flies examined was the same as in Fig. 1E. (C) The difference between the largest and smallest h_i (i.e. $\langle\cos6\theta_j\rangle$) among adjacent cells is denoted as D_i. Note that D_i is defined for both hexagonal and nonhexagonal cells. Cumulative frequencies of D_i for hexagonal (red) and nonhexagonal (blue) cells in numerical simulation or at the stages indicated are shown. The values of parameters in numerical simulation were the same as those employed in Fig. 3H. From 21 to 23 hours APF, the distributions of D_i were almost identical between hexagonal and nonhexagonal cells ($P=0.21$, Wilcoxon rank sum test). During the later stages, D_i for nonhexagonal cells was increased whereas that for hexagonal cells was not ($P<10^{-8}$). The fly genotype was *sqhp-sqhGFP*, *apterous-gal4/sqhp-sqhGFP*, *UAS-Dα-catenin-TagRFP*. Scale bar: 20 μm.

multicellular pattern formation; the maximum stress direction at the tissue level provided directional information for assignment of the orientation of hexagonal cells, leading to the organization of the hexagonally packed, structurally stable wing (supplementary material Fig. S12B, arrows 2 and 3).

As anisotropic stress of the wing emerges from the hinge constriction, mechanical interactions between different tissues or body parts can serve as input for the mechanical processes of cells and molecules. Such passive mechanical reactions affect the active mechanical processes of the force-generating molecular machinery that triggers cell and tissue deformation (Butler et al.,
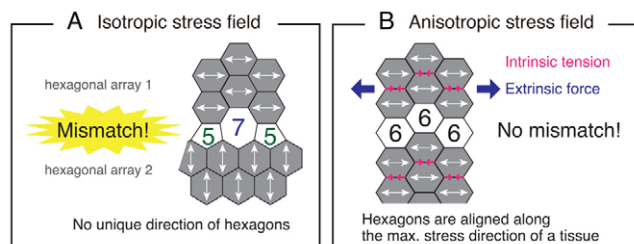
2009; Fernandez-Gonzalez et al., 2009; Pouille et al., 2009; Blanchard and Adams, 2011; Hoffman et al., 2011). Our finding that myosin redistributed in order to resist the extrinsic force in the wing (supplementary material Fig. S12B, arrows 3 and 4) represented one of these feedback processes. Future studies will examine whether similar mechanisms function in cell packing in other epithelial tissues and will further clarify the physical and biological principles behind the active and passive mechanical processes that coordinate multicellular pattern formation and tissue development.

Fig. 9. A physical mechanism of hexagonal cell packing. (**A,B**) Schematics of cell configurations under isotropic (A) and anisotropic (B) stress conditions. In the isotropic condition, nonhexagonal cells appeared between the mismatched top and bottom hexagonal arrays. A large force fluctuation was required to prevent the systems from being trapped in local energy minimum states.

Competing interests statement
The authors declare no competing financial interests.

Author contributions
K.S. and S.I. designed the project, performed data analysis and wrote the paper. K.S. conducted experiments and S.I. conducted numerical simulations.

Supplementary material
Supplementary material available online at
http://dev.biologists.org/lookup/suppl/doi:10.1242/dev.094060/-/DC1

References
Aegerter-Wilmsen, T., Smith, A. C., Christen, A. J., Aegerter, C. M., Hafen, E. and Basler, K. (2010). Exploring the effects of mechanical feedback on epithelial topology. *Development* **137**, 499-506.
Aigouy, B., Farhadifar, R., Staple, D. B., Sagner, A., Röper, J. C., Jülicher, F. and Eaton, S. (2010). Cell flow reorients the axis of planar polarity in the wing epithelium of Drosophila. *Cell* **142**, 773-786.
Batchelor, G. K. (1970). The stress system in a suspension of force-free particles. *J. Fluid Mech.* **41**, 545-570.
Blanchard, G. B. and Adams, R. J. (2011). Measuring the multi-scale integration of mechanical forces during morphogenesis. *Curr. Opin. Genet. Dev.* **21**, 653-663.
Bonnet, I., Marcq, P., Bosveld, F., Fetler, L., Bellaïche, Y. and Graner, F. (2012). Mechanical state, material properties and continuous description of an epithelial tissue. *J. R. Soc. Interface* **9**, 2614-2623.
Bosveld, F., Bonnet, I., Guirao, B., Tlili, S., Wang, Z., Petitalot, A., Marchand, R., Bardet, P. L., Marcq, P., Graner, F. et al. (2012). Mechanical control of morphogenesis by Fat/Dachsous/Four-jointed planar cell polarity pathway. *Science* **336**, 724-727.
Butler, L. C., Blanchard, G. B., Kabla, A. J., Lawrence, N. J., Welchman, D. P., Mahadevan, L., Adams, R. J. and Sanson, B. (2009). Cell shape changes indicate a role for extrinsic tensile forces in Drosophila germ-band extension. *Nat. Cell Biol.* **11**, 859-864.
Chiou, K. K., Hufnagel, L. and Shraiman, B. I. (2012). Mechanical stress inference for two dimensional cell arrays. *PLOS Comput. Biol.* **8**, e1002512.
Classen, A. K., Anderson, K. I., Marois, E. and Eaton, S. (2005). Hexagonal packing of Drosophila wing epithelial cells by the planar cell polarity pathway. *Dev. Cell* **9**, 805-817.
Cooper, M. A., Son, A. I., Komlos, D., Sun, Y., Kleiman, N. J. and Zhou, R. (2008). Loss of ephrin-A5 function disrupts lens fiber cell packing and leads to cataract. *Proc. Natl. Acad. Sci. USA* **105**, 16620-16625.
Dahmann, C., Oates, A. C. and Brand, M. (2011). Boundary formation and maintenance in tissue development. *Nat. Rev. Genet.* **12**, 43-55.
Eaton, S. and Jülicher, F. (2011). Cell flow and tissue polarity patterns. *Curr. Opin. Genet. Dev.* **21**, 747-752. (I).
Farhadifar, R., Röper, J. C., Aigouy, B., Eaton, S. and Jülicher, F. (2007). The influence of cell mechanics, cell-cell interactions, and proliferation on epithelial packing. *Curr. Biol.* **17**, 2095-2104.
Fernandez-Gonzalez, R., Simoes, S. M., Röper, J. C., Eaton, S. and Zallen, J. A. (2009). Myosin II dynamics are regulated by tension in intercalating cells. *Dev. Cell* **17**, 736-743.
Fisher, N. I. (1993). *Statistical Analysis of Circular Data.* Cambridge: Cambridge University Press.
Fristrom, D. and Fristrom, J. W. (1993). The metamorphic development of the adult epidermis. In *The Development of Drosophila Melanogaster* (ed. M. Bate and A. Martinez Arias), pp. 843-897. Cold Spring Harbor, NY: Cold Spring Harbor Laboratory Press.
Graner, F. and Sawada, Y. (1993). Can surface adhesion drive cell rearrangement? Part II: a geometrical model. *J. Theor. Biol.* **164**, 477-506.
Hales, T. C. (2001). The honeycomb conjecture. *Discrete Comput. Geom.* **25**, 1-22.
Hoffman, B. D., Grashoff, C. and Schwartz, M. A. (2011). Dynamic molecular processes mediate cellular mechanotransduction. *Nature* **475**, 316-323.
Honda, H. (1983). Geometrical models for cells in tissues. *Int. Rev. Cytol.* **81**, 191-248.
Honda, H., Motosugi, N., Nagai, T., Tanemura, M. and Hiiragi, T. (2008). Computer simulation of emerging asymmetry in the mouse blastocyst. *Development* **135**, 1407-1414.
Huang, J., Zhou, W., Dong, W., Watson, A. M. and Hong, Y. (2009). From the Cover: Directed, efficient, and versatile modifications of the Drosophila genome by genomic engineering. *Proc. Natl. Acad. Sci. USA* **106**, 8284-8289.
Hutson, M. S., Tokutake, Y., Chang, M. S., Bloor, J. W., Venakides, S., Kiehart, D. P. and Edwards, G. S. (2003). Forces for morphogenesis investigated with laser microsurgery and quantitative modeling. *Science* **300**, 145-149.

Ishihara, S. and Sugimura, K. (2012). Bayesian inference of force dynamics during morphogenesis. *J. Theor. Biol.* **313**, 201-211.
Ishihara, S., Sugimura, K., Cox, S. J., Bonnet, I., Bellaïche, Y. and Graner, F. (2013). Comparative study of non-invasive force and stress inference methods in tissue. *Eur. Phys. J. E* **36**, 45.
Käfer, J., Hayashi, T., Marée, A. F., Carthew, R. W. and Graner, F. (2007). Cell adhesion and cortex contractility determine cell patterning in the Drosophila retina. *Proc. Natl. Acad. Sci. USA* **104**, 18549-18554.
Kasza, K. E. and Zallen, J. A. (2011). Dynamics and regulation of contractile actin-myosin networks in morphogenesis. *Curr. Opin. Cell Biol.* **23**, 30-38.
Kiehart, D. P., Lutz, M. S., Chan, D., Ketchum, A. S., Laymon, R. A., Nguyen, B. and Goldstein, L. S. (1989). Identification of the gene for fly non-muscle myosin heavy chain: *Drosophila* myosin heavy chains are encoded by a gene family. *EMBO J.* **8**, 913-922.
Knox, A. L. and Brown, N. H. (2002). Rap1 GTPase regulation of adherens junction positioning and cell adhesion. *Science* **295**, 1285-1288.
Koto, A., Kuranaga, E. and Miura, M. (2009). Temporal regulation of Drosophila IAP1 determines caspase functions in sensory organ development. *J. Cell Biol.* **187**, 219-231.
Lecuit, T. and Lenne, P. F. (2007). Cell surface mechanics and the control of cell shape, tissue patterns and morphogenesis. *Nat. Rev. Mol. Cell Biol.* **8**, 633-644.
Lecuit, T., Lenne, P. F. and Munro, E. (2011). Force generation, transmission, and integration during cell and tissue morphogenesis. *Annu. Rev. Cell Dev. Biol.* **27**, 157-184.
Ma, D., Amonlirdviman, K., Raffard, R. L., Abate, A., Tomlin, C. J. and Axelrod, J. D. (2008). Cell packing influences planar cell polarity signaling. *Proc. Natl. Acad. Sci. USA* **105**, 18800-18805.
Mofrad, M. R. K. and Kamm, R. D. (2006). *Cytoskeletal Mechanics.* Cambridge: Cambridge University Press.
Nienhaus, U., Aegerter-Wilmsen, T. and Aegerter, C. M. (2009). Determination of mechanical stress distribution in Drosophila wing discs using photoelasticity. *Mech. Dev.* **126**, 942-949.
O'Keefe, D. D., Gonzalez-Niño, E., Edgar, B. A. and Curtiss, J. (2012). Discontinuities in Rap1 activity determine epithelial cell morphology within the developing wing of Drosophila. *Dev. Biol.* **369**, 223-234.
Oda, H., Uemura, T., Harada, Y., Iwai, Y. and Takeichi, M. (1994). A Drosophila homolog of cadherin associated with armadillo and essential for embryonic cell-cell adhesion. *Dev. Biol.* **165**, 716-726.
Ouchi, N. B., Glazier, J. A., Rieu, J. P., Upadhyaya, A. and Sawada, Y. (2003). Improving the realism of the cellular Potts model in simulations of biological cells. *Physica A* **329**, 451-458.
Paluch, E. and Heisenberg, C. P. (2009). Biology and physics of cell shape changes in development. *Curr. Biol.* **19**, R790-R799.
Pouille, P. A., Ahmadi, P., Brunet, A. C. and Farge, E. (2009). Mechanical signals trigger Myosin II redistribution and mesoderm invagination in Drosophila embryos. *Sci. Signal.* **2**, ra16.
Raphael, Y. and Altschuler, R. A. (2003). Structure and innervation of the cochlea. *Brain Res. Bull.* **60**, 397-422.
Rauzi, M., Verant, P., Lecuit, T. and Lenne, P. F. (2008). Nature and anisotropy of cortical forces orienting Drosophila tissue morphogenesis. *Nat. Cell Biol.* **10**, 1401-1410.
Royou, A., Field, C., Sisson, J. C., Sullivan, W. and Karess, R. (2004). Reassessing the role and dynamics of nonmuscle myosin II during furrow formation in early Drosophila embryos. *Mol. Biol. Cell* **15**, 838-850.
Sano, H., Kunwar, P. S., Renault, A. D., Barbosa, V., Clark, I. B., Ishihara, S., Sugimura, K. and Lehmann, R. (2012). The Drosophila actin regulator ENABLED regulates cell shape and orientation during gonad morphogenesis. *PLoS ONE* **7**, e52649.
Shimada, Y., Yonemura, S., Ohkura, H., Strutt, D. and Uemura, T. (2006). Polarized transport of Frizzled along the planar microtubule arrays in Drosophila wing epithelium. *Dev. Cell* **10**, 209-222.
Strutt, H. and Strutt, D. (2009). Asymmetric localisation of planar polarity proteins: Mechanisms and consequences. *Semin. Cell Dev. Biol.* **20**, 957-963.
Sugimura, K., Bellaïche, Y., Graner, F., Marcq, P. and Ishihara, S. (2013). Robustness of force and stress inference in an epithelial tissue. *Conf. Proc. IEEE Eng. Med. Biol. Soc.* (in press)
Thompson, D. W. (1917). *On Growth and Form.* Cambridge: Cambridge University Press.
Usui, T., Shima, Y., Shimada, Y., Hirano, S., Burgess, R. W., Schwarz, T. L., Takeichi, M. and Uemura, T. (1999). Flamingo, a seven-pass transmembrane cadherin, regulates planar cell polarity under the control of Frizzled. *Cell* **98**, 585-595.
Wootton, R. J. (1992). Functional morphology of insect wings. *Annu. Rev. Entomol.* **37**, 113-140.

Development

Fig. S1. Quantification of orientation of hexagonal cells. (**A**) Orientation of a hexagonal cell is characterized by $\langle \cos 6\theta_j \rangle$ (the average of $\cos 6\theta_j$, where θ_{1-6} represents the angles of the edges belonging to the cell). The PD and AP oriented hexagons are colored blue and yellow, respectively. (**A′**) Hexagonal cells are color-coded by $\langle \cos 6\theta_j \rangle$ in the control wing at 35 hours APF. Nonhexagonal cells are shown in black. The $\langle \cos 6\theta_j \rangle$ map illustrates the segregation of hexagonal cell arrays. (**B**) Orientation of a cell shape anisotropy, φ, is defined by the angle of the longest axis of a fitted ellipse. The angle is defined between 0 and π. (**B′**) Cells shown in A′ are color-coded by $\cos\varphi$. The segregation of hexagonal cell arrays is not clearly detected. The fly genotype is as described in the legend of Fig. 1.

Fig. S2. Developmental changes in the distribution of inferred tension and the myosin subunit in the wing. (**A-E**) Patterns of the estimated tension at the stages indicated. In B, the arrows indicate the PD and AP edges. (**A′-E′**) The direction of each edge is classified (e.g. red class I for the PD edges and blue class III for the AP edges) and its estimated tension is plotted against its length. The longest axis of the stress ellipse represents the maximum stress direction of a group of cells. (**A″-E″**) Images of the wing expressing MRLC-GFP under the control of a promoter of the *MRLC* gene (A″-E″) and a cell shape marker (Dα–catenin-TagRFP) (A‴-E‴) at the stages indicated. The yellow and blue arrowheads indicate the PD and AP edges, respectively. Actin-GFP did not show a strongly biased distribution (data not shown). (A⁗-E⁗) Quantification of the mean signal intensity of MRLC-GFP (bar, left *y*-axis) and the average length of the edges (line, right *y*-axis) for each angle class. (**F**) A wing at 24 hours APF stained for anti-Zipper (myosin heavy chain) and anti-DECadherin. The yellow and blue arrowheads indicate the PD and AP edges, respectively. Zipper is enriched on the PD edges, as is MRLC-GFP. Only a low level of phosphor-myosin was detected (data not shown). (**G**) The MRLC-GFP signal intensity of each edge (arbitrary units) is plotted against its length in each angular class for data shown in B″. (**H**) The correlation between myosin and the edge length of the class III edges is shown. The number of samples examined is indicated. Class I, II and IV edges had similar values to class III edges (data not shown). The fly genotypes are as described in the legend of Fig. 1 (A-E,G,H), and *DEcadherin-GFP* knock-in (F). Scale bars: 20 μm (A,A″) and 5 μm (F).

Fig. S3. Statistical analysis of the angular bias of inferred tension, edge length and MRLC signal intensity. (**A**) The anisotropy of the MRLC-GFP signal intensity is represented by R_S, $R_S\langle s \rangle e^{i2\Theta} = \langle se^{i2\theta} \rangle - \langle s \rangle\langle e^{i2\theta} \rangle$, where s_{ij} and θ_{ij} ($0 \leq \theta_{ij} < \pi$) are the MRLC-GFP signal intensity and the angle of the contact surface between the ith and jth cells, respectively. R_S decreases if the signal intensity is uncorrelated with respect to the orientation of the edges. The anisotropy of the inferred tension (R_T) and that of the edge length (R_L) were evaluated using the same procedures. See supplementary material Fig. S4 for their statistical significance. (**B-B″**) The anisotropy of the inferred tension (R_T; B), the length of the edge (R_L; B′) and the MRLC-GFP signal intensity (R_S; B″) were plotted [red: wing (data shown in Fig. S2); blue: scutum]. The number of samples examined is indicated. The fly genotype is as described in the legend of Fig. 1.

Fig. S4. Statistical significance of the angular bias of inferred tension, edge length and MRLC signal intensity in the wing. (**A**) A bootstrap method for evaluating *P* values. Briefly, starting from the observed data set $\{s_{ij}, \theta_{ij}\}$ (red lines), we generated a bootstrap sample $\{s'_{ij}, \theta_{ij}\}$ by randomly assigning a signal intensity to each edge from $\{s_i\}$ and calculating R_S. Repeating this process 10,000 times, we obtained the distribution for the bootstrap samples (green curve). (**B-F″**) Data shown in Figs S2, S3 were analyzed to check the statistical significance by evaluating *P* values using a bootstrap method. We obtained a distribution for R_S. R_T, R_L, and R_S for the observed data for the wing at various developmental stages (lines), plotted together with their distribution for the bootstrap samples (green curves; B-F, B′-F′ and B″-F″, respectively). R_T, R_L, and R_S are normalized to their mean values. In each figure, the statistical significance of R is represented by colored lines (red: $P<0.01$; gray: $P\geq0.01$). Inset: the directions of R_T, R_L, and R_S are plotted (red: $P<0.01$; gray: $P\geq0.01$). R_S was not polarized toward a particular direction (i.e., bias direction Θ_S) at 13-14 hours APF (inset in B″). However, at 16.5-23 hours APF, all of the samples were aligned parallel to the PD axis (insets in C″,D″). They then gradually separated at later stages (insets in E″,F″). A bootstrap test indicated that the R_S of almost all of the samples was statistically significant at 16.5-23 hours APF (C″,D″). By contrast, more gray lines representing $P\geq0.01$ can be seen at other stages (B″,E″,F″).

Fig. S5. Cell junction tension measured by response to laser ablation of single cell contact surface. (**A-E′**) The response to laser cutting of single cell contact surface at the stages indicated was examined as was previously reported (Aigouy et al., 2010; Ishihara and Sugimura, 2012).

Each circle represents one ablated edge plotted on a 2D plane according to its length and direction at different stages. 0 and π correspond to the PD direction (see the number of angle classes). The color of the circle indicates the initial velocity of vertices, which was measured by the displacement of vertices 16 seconds after laser irradiation. For edges of a similar length, displacement was larger at the PD edges than at the AP edges at every stage, except at 13-14 hours APF. These developmental changes were also observed when we quantified the displacement of the vertices at 71 seconds. The number of edges analyzed is shown in the upper right-hand corner. (D′,E′) The tension of an edge was estimated from image data just before cutting the edge as was done in Ishihara and Sugimura, 2012. The inferred tension plotted against V_{max} of the vertices in wings at 25.5-27.5 hours APF (D′) and 30-32 hours APF (E′). The correlation coefficient was 0.80 (25.5-27.5 hours APF) and 0.60 (30-32 hours APF). Results of the analysis at 16.5-18.5 hours APF were published previously (Ishihara and Sugimura, 2012). The fly genotype is as described in the legend of Fig. 1.

Fig. S6. Developmental changes in the anisotropy of global stress. (**A**) Developmental changes in the inferred normal stress difference $\sigma_A \equiv (\sigma_{xx} - \sigma_{yy})/2$ in control wings. The number of samples examined is indicated. (**B**) The inferred σ_A plotted against $V_x - V_y$ measured by global ablation of tissue (as in Fig. 2F and Movies 1, 2) for wings at 22 hours APF (red), 26 hours APF (black), 30 hours APF (magenta) and scutum (blue). σ_A was calibrated by the average V_{max} of the vertices after cutting single cell contact surface at corresponding stages. The correlation coefficient was 0.88 with calibration and 0.73 without calibration. The fly genotype was *DEcadherin-GFP* knock-in.

Fig. S7. Anisotropic stress promotes hexagonal packing. (**A-D**) In addition to cutting the wing by forceps as was done in Figs 3 and 4, we also employed a different way of relaxing tissue stretch; a two-photon laser cut the wing along the anterior cross vein at 23.5-24 hours APF. (**A,B**) Images of pupal wings at 34.5-35.5 hours APF. In B, the wing was severed by a femtosecond laser at 23.5 hours APF. The percentage of hexagonal cells was: 72.8 % (A) and 57.1 % (B). (**C**) Quantification of the fraction of hexagonal cells in the control and cut wings. (**D**) The average value of $\langle \cos 6\theta_j \rangle$ in each wing or wing cut at 23.5-24 hours APF is calculated, and mean ± s.d. among samples at each developmental stage is plotted. The fly genotype is as described in the legend of Fig. 1.

Fig. S8. Directional bias in stress is crucial for hexagonal packing in a numerical simulation of cell rearrangement. (**A**) Mechanical processes in a cell. Currently, three processes are considered to underlie pressure and tension: (1) area elasticity, (2) cell adhesion and (3) contraction. Each process can be expressed as a form of potential energy, and minimization of the potential is expected to determine the geometry of the cells. A and L are the area and peripheral length of a cell at the plane of the adherens junction, respectively. l is the length of the contact surface between the cells. (**B**) Time evolution of the fraction of hexagonal cells for noise intensity $z = 1, 10, 30$ and 50%. The results of the simulations under no stretch, isotropic stretch and horizontal stretch are indicated with green, blue and red lines, respectively. The parameters were set as follows: $\tilde{\sigma}_0 = 0.12$; $\tilde{\Lambda} = 0.04$, and $1/\tau = 0.1$ (see equations S2-2 and S2-5 in Appendix S1). (**C**) Fractions of hexagonal cells at $t = 2000$ in the numerical simulations are plotted against noise intensity (z) for several values of τ ($\tilde{\sigma}_0 = 0.12$) ($n=8$ for each set of parameters). The results of the simulations under no extrinsic force, isotropic stretch and horizontal stretch are indicated with squares, crosses and circles, respectively. (**D,E**) Results of simulations under (D) isotropic and (E) horizontal stretch. Left: the newly formed edges through cell-cell intercalation are shown by the magenta lines. Right: angular distribution of the newly formed edges ($n=20$ for each condition).

Fig. S9. The RNAi against *sqh* results in the excess shear deformation of wing cells. (**A,B**) Dα-catenin-TagRFP images of control wing (A) and wing expressing a dsRNA targeting *sqh* that encodes MRLC (B). Yellow dots label corresponding cells. Control and *sqh* RNAi embryos and larvae were raised at 21°C and third instar larvae were switched to 29°C to induce the expression of dsRNA against *sqh*. After 24 hours, white pupae were picked for analysis. Time-lapse imaging was conducted at 21-22 hours APF at 29°C, which corresponds to ~24-25 hours APF at 25°C. In B, excess shear deformation of cells was observed. Over the twenty minutes observation shown (B), and in the 1-hour time-lapse movie (not shown), cell rearrangement was suppressed. When embryos and larvae were raised at 21°C and white pupae were switched to 29°C, excess shear deformation of cells was not observed, and cell rearrangement was biased along the PD axis (refer to the main text). The decrease of MRLC level in the *sqh* RNAi flies was confirmed (data not shown). (**C**) Mechanical force balance in the *Drosophila* pupal wing.

The intrinsic cell junction tension generated by myosin resists the extrinsic tissue stretch. Inferred tension and myosin signal intensity were negatively correlated with the length of cell contact surface in each angle class (supplementary material Fig. S2A′-E′,G,H) as expected from the force-generating property of myosin. On the other hand, the extrinsic force elongates cell contact surfaces. The fly genotypes were *patched-gal4, tubP-gal80^{ts}/sqhp-sqhGFP, UAS-Dα–catenin-TagRF*; +/+ (A), and *patched-gal4, tubP-gal80^{ts}/sqhp-sqhGFP, UAS-Dα–catenin-TagRF*; *UAS-sqh dsRNA/+* (B). (C) Scale bar: 20 μm (B).

Fig. S10. Temporal changes in the anisotropy of local cell stress during hexagonal cell packing. (**A**,**B**) The developmental changes in local cell stress. Time-lapse data obtained from 23.5 to 30.5 hours APF were extracted at 3-minute intervals. (A) Each cell is differentially colored by its anisotropy of local cell stress (color bar; *a/b* in Fig. 5A). The coefficient of variation (CV; the standard deviation/the mean) of the aspect ratio of local cell stress ellipse among cells #1-#4 is indicated at the bottom right of each panel. (B) The aspect ratio of local cell stress ellipse is quantified before and after the PD intercalation of cells. Its CV among four cells that are involved in the PD intercalation is plotted. (**C**) Balance of the extrinsic forces (blue arrows) and intrinsic contracting forces (pink arrows). An edge with tension T, length l and angle θ contributes to N_{xx} as ~ $Tl\cos^2\theta/a_e$ along the x-axis, where a_e represents an area that the edge supports. It indicates that the tension along the horizontal edges (top) is able to more efficiently counteract the horizontal stretch than the tension of the vertical edges (bottom). It is thus suggested that the PD intercalation of cells (i.e., an increase of the PD edges) lowers the average magnitude of tension on PD edges. The fly genotype is as described in the legend of Fig. 1. Scale bar: 5 μm (B).

Fig. S11. In *flamingo* (*fmi*) RNAi wing, hexagonal packing proceeded normally until 27.5 h APF, but was disrupted afterwards. (**A-A″**) The anisotropy of the inferred tension (R_T; A), the length of the edge (R_L; A′), and the MRLC-GFP signal intensity (R_S; A″) were plotted [red: wing (data shown in Fig. S2), magenta: *fmi* RNAi wing]. The number of samples examined is indicated. Inferred tension, myosin localization and cell elongation exhibited normal developmental changes in *fmi* RNAi wings. The standard deviations of the magnitude (*c* in Fig. 5A) and anisotropy (*a − b* in Fig. 5A) of inferred local cell stress at 25.5-27.5 hours APF were 0.095±0.013 and 1.10±0.19 in control wing, and they were 0.095±0.013 and 1.17±0.14 in *fmi* RNAi wing. The standard deviation of inferred tension at 25.5-27.5 hours APF was 0.158±0.020 and 0.168±0.014 in the control and *fmi* RNAi wings, respectively. The PD biased localization of myosin was observed in two other conditions, in which PCP was disputed: a homogeneous viable null allele of *prickle* (*prickle^1*) (Gubb et al, 1999) and overexpression of *fat* by ptc-gal4 (Ma et al., 2003; Matakatsu and Blair, 2004) (data not shown). (**B**,**C**) Developmental changes in cell packing and alignment are compared between control and *fmi* RNAi wings. The number of control flies examined is indicated. (B) The fraction of hexagonal cells in control (red) and *fmi* RNAi (magenta) wings. (C) The orientation of the edges of each hexagonal cell is quantified by $\langle\cos6\theta_j\rangle$ as in Fig. 1G, and the average of the values among samples is plotted (red: control, and magenta; *fmi* RNAi). Genotype of control fly is as described in the legend of Fig. 1, and that of the *fmi* RNAi fly is *sqhp-sqhGFP, apterous-gal4/sqhp-sqhGFP, UAS-Dα–catenin-TagRFP*; *UAS-fmi dsRNA/+*.

Fig. S12. Summary of tissue mechanics and cell-level dynamics that underlie hexagonal cell packing. (**A**) Tissue mechanics, cell-level dynamics and hexagonal cell packing in the *Drosophila* pupal wing (Classen et al., 2005; Aigouy et al., 2010; this study). Strong anisotropy of tissue stress is present until early phase II, when the anisotropies of cell junction tension and myosin have started decreasing. This strong tissue stress anisotropy triggers the directional alignment of hexagonal cells along the tissue-stretching direction. (**B**) Mechanical regulation of hexagonal pattern formation connecting molecular, cellular and tissue (cell-population) dynamics. Arrow 1: Myosin controls the mechanical properties of a cell and generates contracting tension to trigger junction remodeling. Arrow 2: Directional cell rearrangement promotes hexagonal packing. Arrow 3: The stress field (i.e., the maximum stress direction) of a tissue provides directional information for the alignment of individual cells. Arrows 3 and 4: A cell senses the stress field of the tissue and modifies its distribution of myosin.
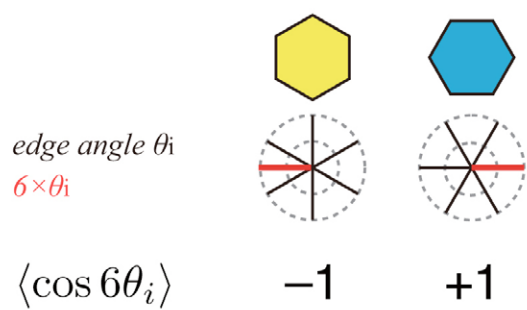
Movie 1. Ablation of a group of cells in the wing. A wing at 22 hours APF. Anterior is up and proximal is left. Cells at the center were ablated. The anisotropic extension of cell group contour confirmed the PD bias of global stress in the wing. Time label of the movie is: 14", -4", 4", 14", 24", … , 214" (laser irradiation was at 0 seconds). The fly genotype is *DEcadherin-GFP* knock-in. Scale bar: 20 μm.

Movie 2. Ablation of a group of cells in the scutum. A scutum at 22 hours APF. Anterior is left. Cells at the center were ablated. Note that the anisotropy in the outward velocity of cells was smaller in the scutum than in the wing (compare Movies 1 and 2). The time label of the movie and fly genotype are as described in the legend of Movie 1. Scale bar: 20 μm.

Movie 3. Temporal dynamics of the inferred tensions. Time-lapse images were taken from 23.5-30.5 hours APF, and data from 25-26 hours APF were extracted at 3-minute intervals. The arrowheads and arrows point to the AP and PD edges, respectively. The fly genotype is as described in the legend of Fig. 1.

A "Orientation of cell contact surface"

edge angle θ_i
$6 \times \theta_i$

$\langle \cos 6\theta_i \rangle$ -1 $+1$

B "Orientation of cell shape anisotropy"

Angle of longest axis of ellipse ϕ

$\cos \phi$ 0 $+1$

$-\pi/2 \leq \phi \leq \pi/2$

A′

-1 0 1

Black: non-hexagonal cells
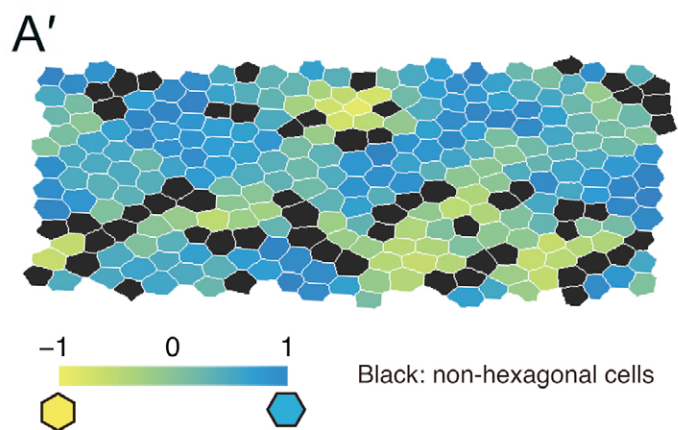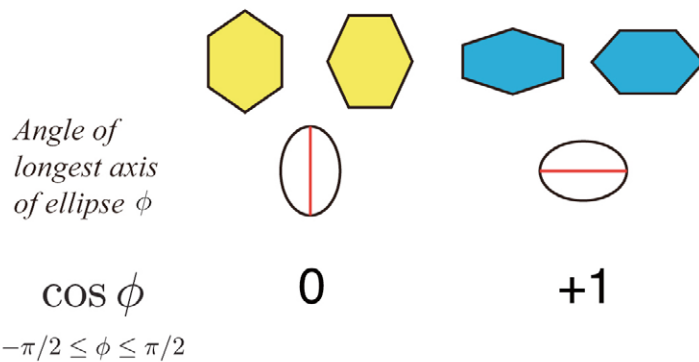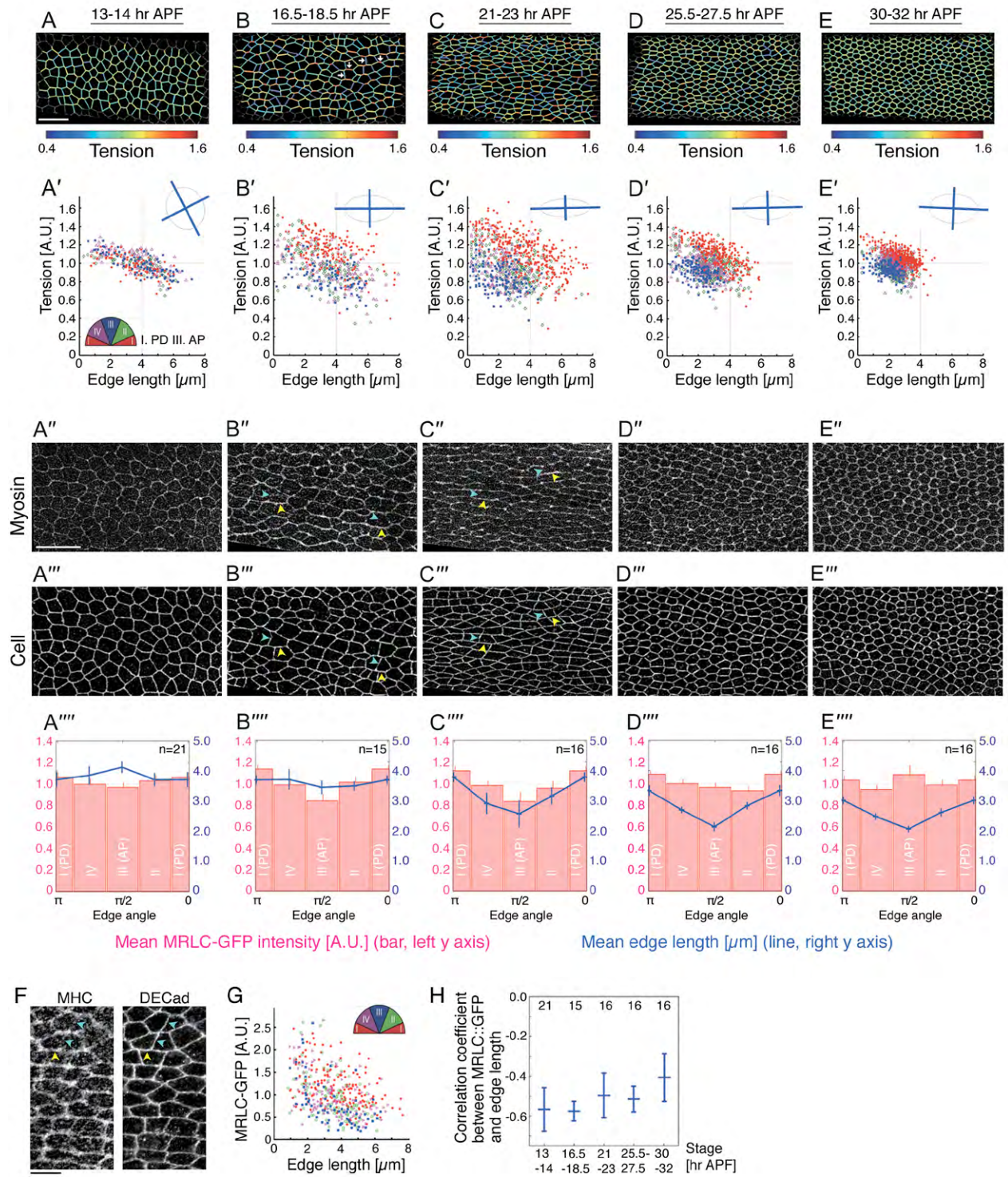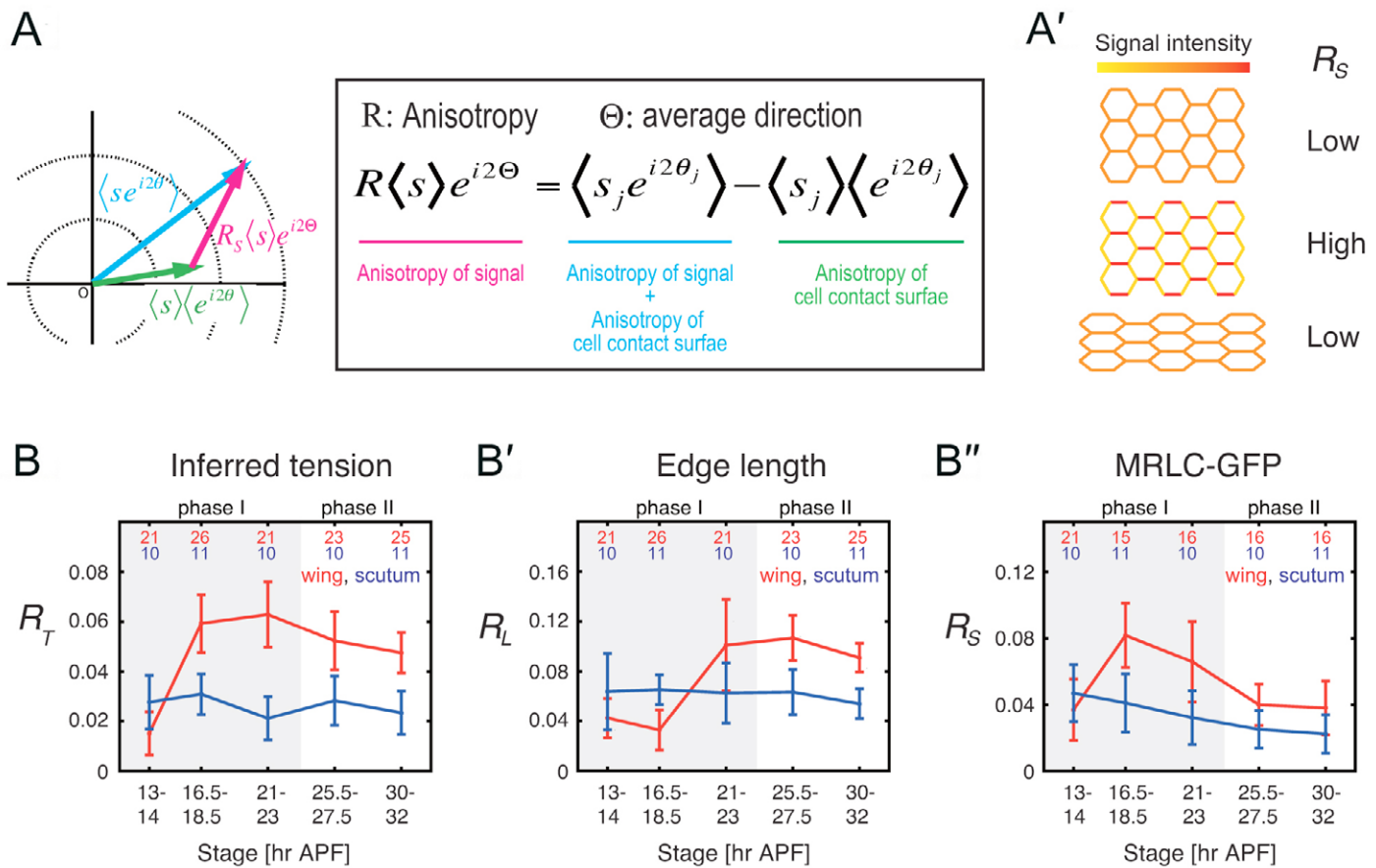
B′

1 0 1

Gray: non-hexagonal cells
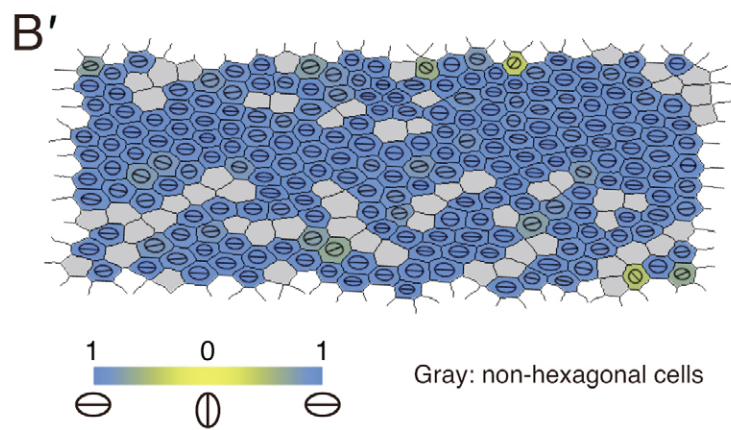
Fig. S1. Quantification of orientation of hexagonal cells.
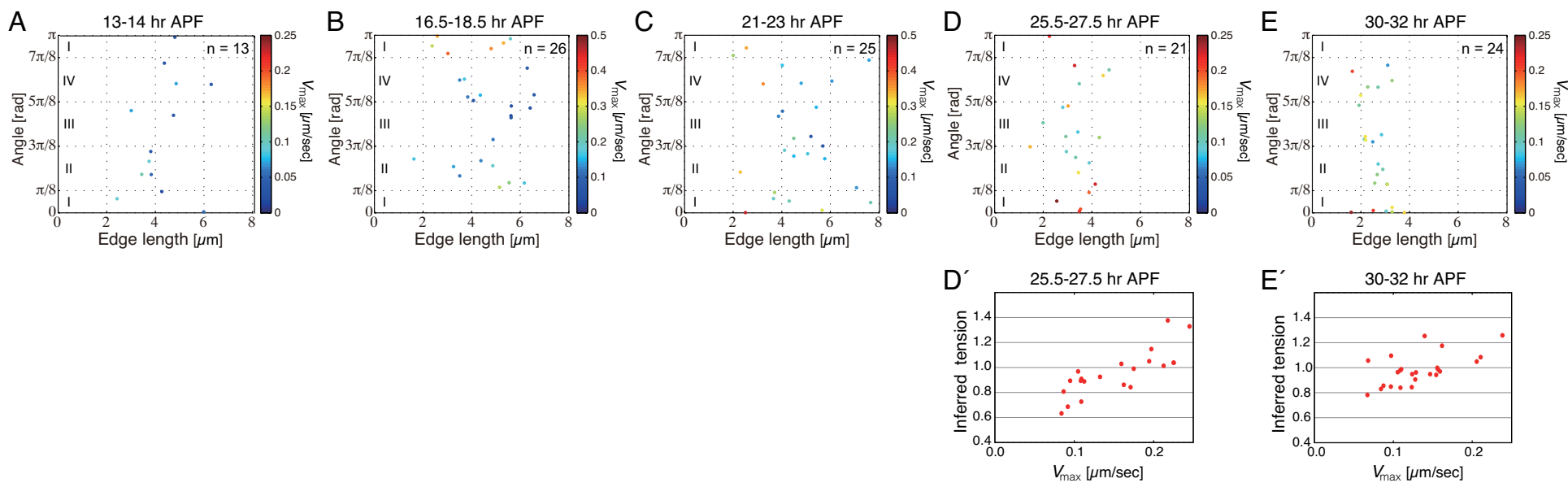
Fig. S2. Developmental changes in the distribution of inferred tension and the myosin subunit in the wing.

Fig. S3. Statistical analysis of the angular bias of inferred tension, edge length and MRLC signal intensity.

Fig. S5. Cell junction tension measured by response to laser ablation of single cell contact surface.
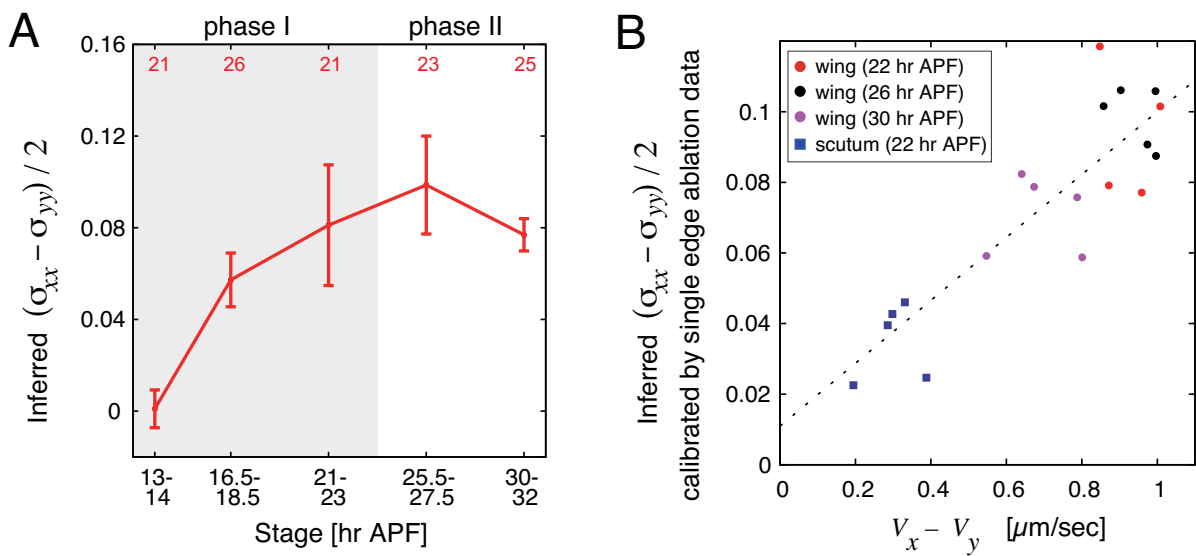
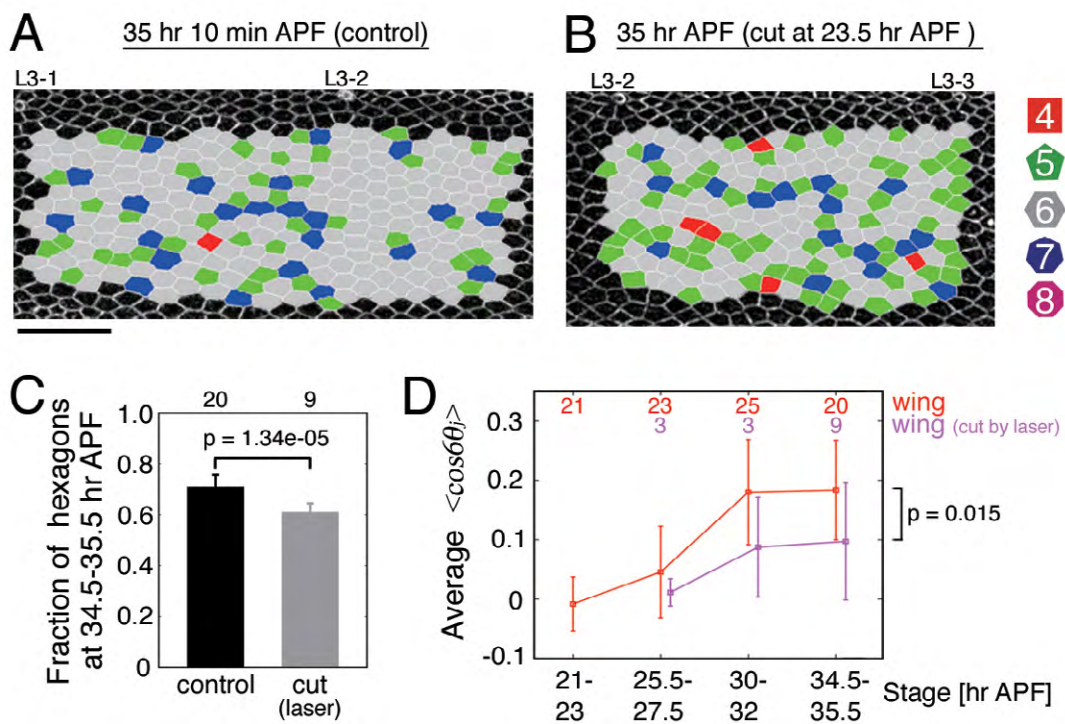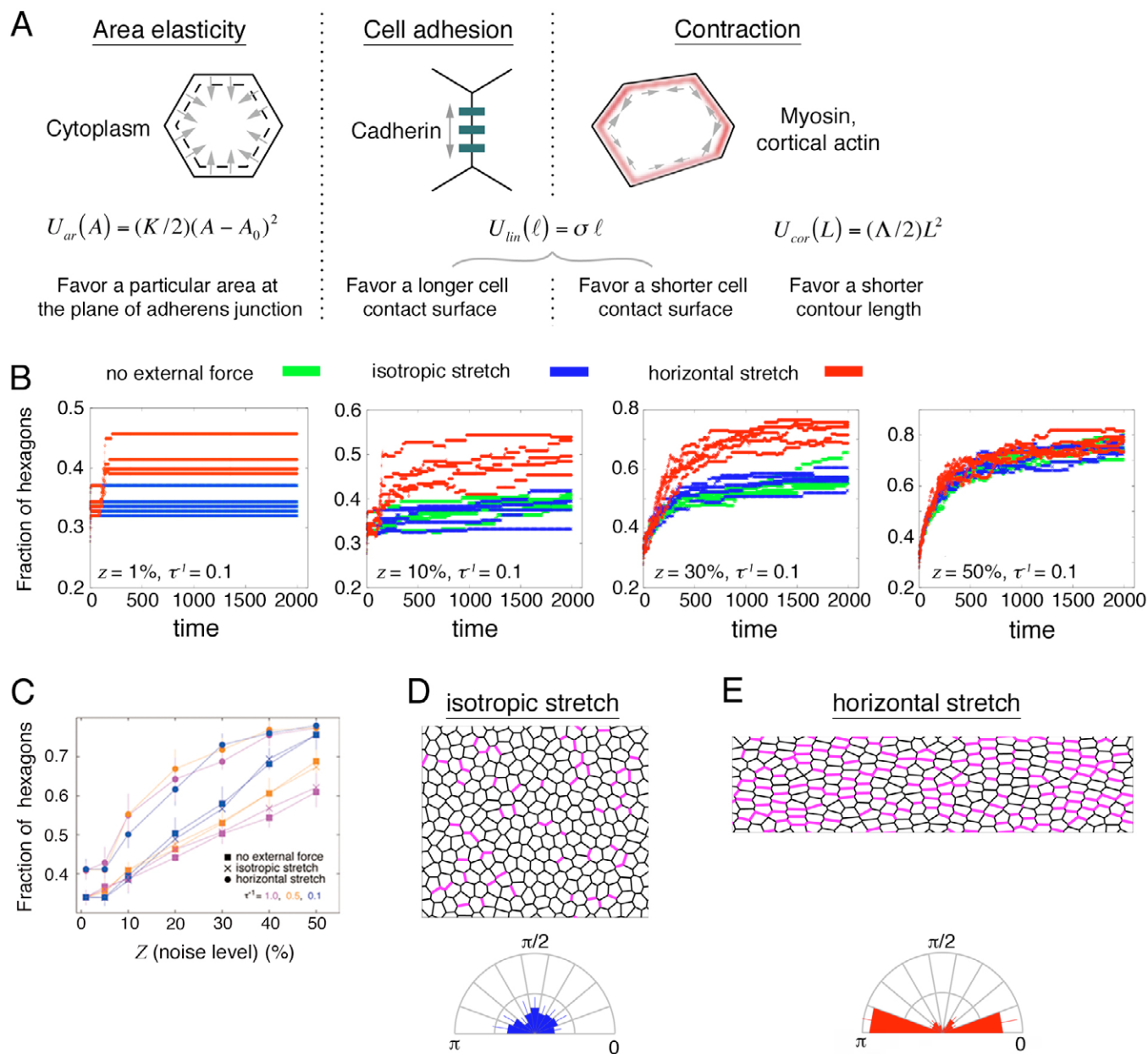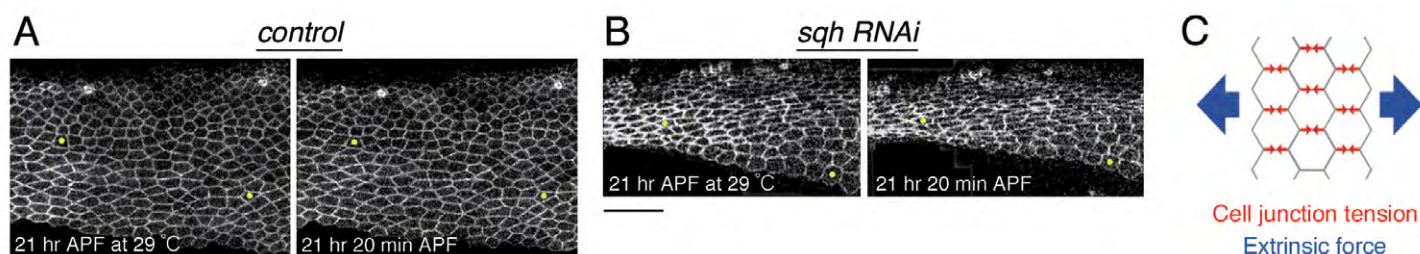Fig. S6. Developmental changes in the anisotropy of global stress.

Fig. S7. Anisotropic stress promotes hexagonal packing.

A

Area elasticity

Cytoplasm

$$U_{ar}(A) = (K/2)(A - A_0)^2$$

Favor a particular area at the plane of adherens junction

Cell adhesion

Cadherin

$$U_{lin}(\ell) = \sigma \ell$$

Favor a longer cell contact surface

Favor a shorter cell contact surface

Contraction

Myosin, cortical actin

$$U_{cor}(L) = (\Lambda/2)L^2$$

Favor a shorter contour length

B

no external force ■ isotropic stretch ■ horizontal stretch ■

$z = 1\%, \tau^l = 0.1$

$z = 10\%, \tau^l = 0.1$

$z = 30\%, \tau^l = 0.1$

$z = 50\%, \tau^l = 0.1$

Fraction of hexagons / time

C

Fraction of hexagons

Z (noise level) (%)

■ no external force
× isotropic stretch
● horizontal stretch

$\tau^{-1} = 1.0, 0.5, 0.1$

D isotropic stretch

E horizontal stretch

Fig. S8. Directional bias in stress is crucial for hexagonal packing in a numerical simulation of cell rearrangement.

A *control*

21 hr APF at 29 °C   21 hr 20 min APF

B *sqh RNAi*

21 hr APF at 29 °C   21 hr 20 min APF

C

Cell junction tension
Extrinsic force

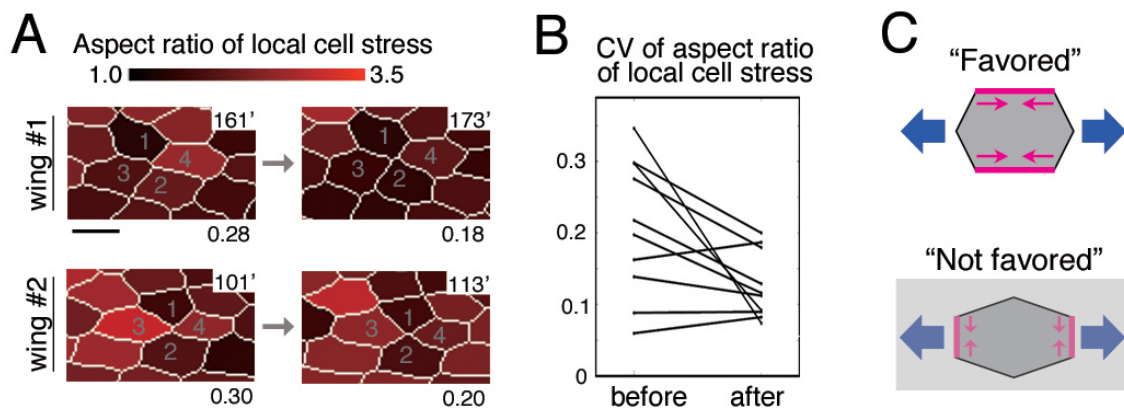**Fig. S9. The RNAi against *sqh* results in the excess shear deformation of wing cells.**

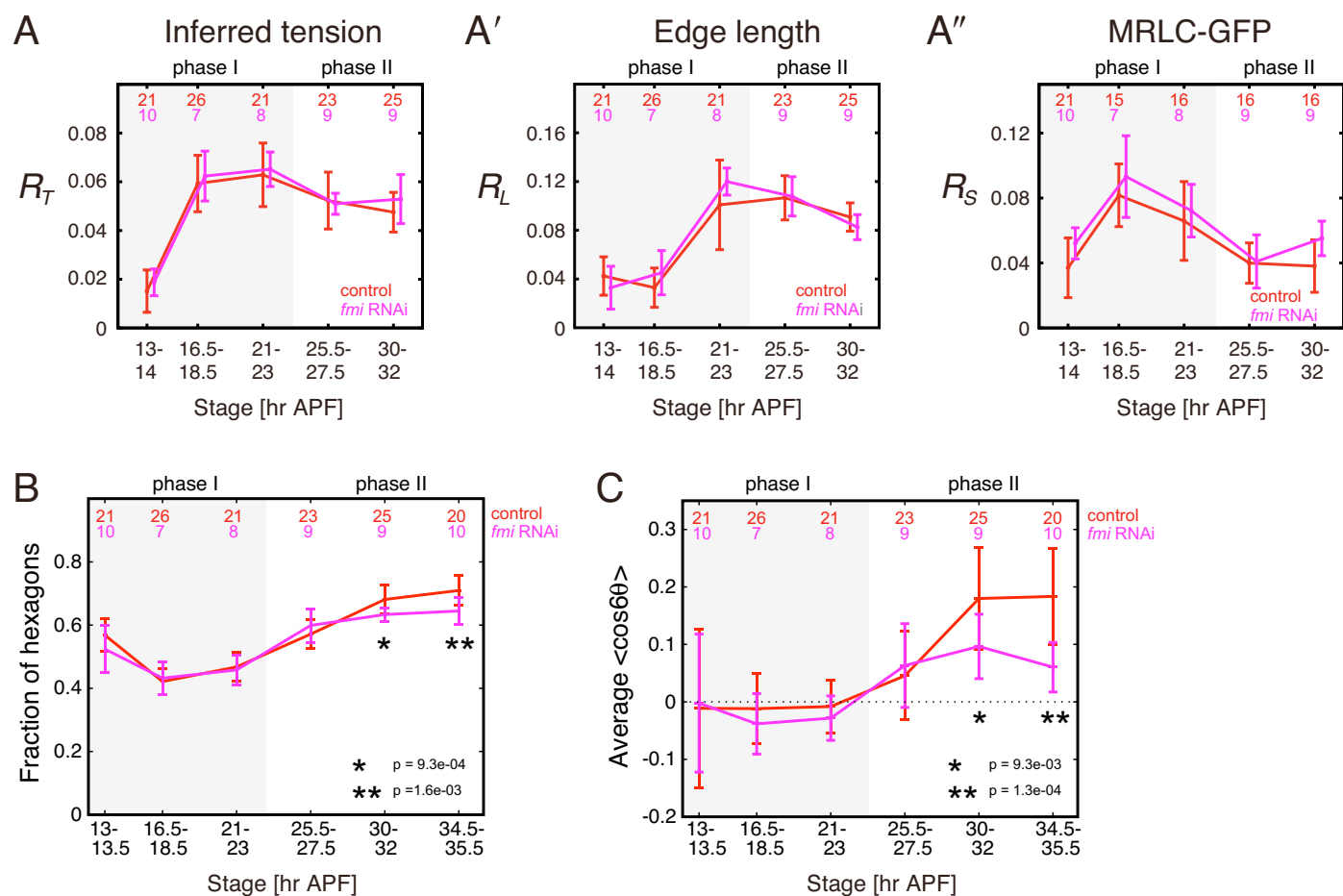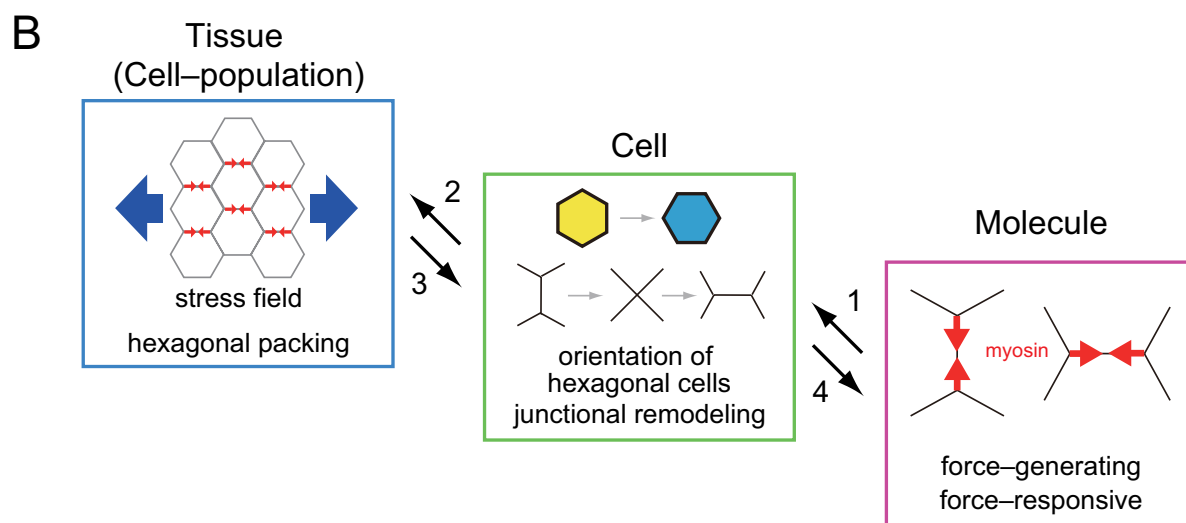**Fig. S10. Temporal changes in the anisotropy of local cell stress during hexagonal cell packing.**
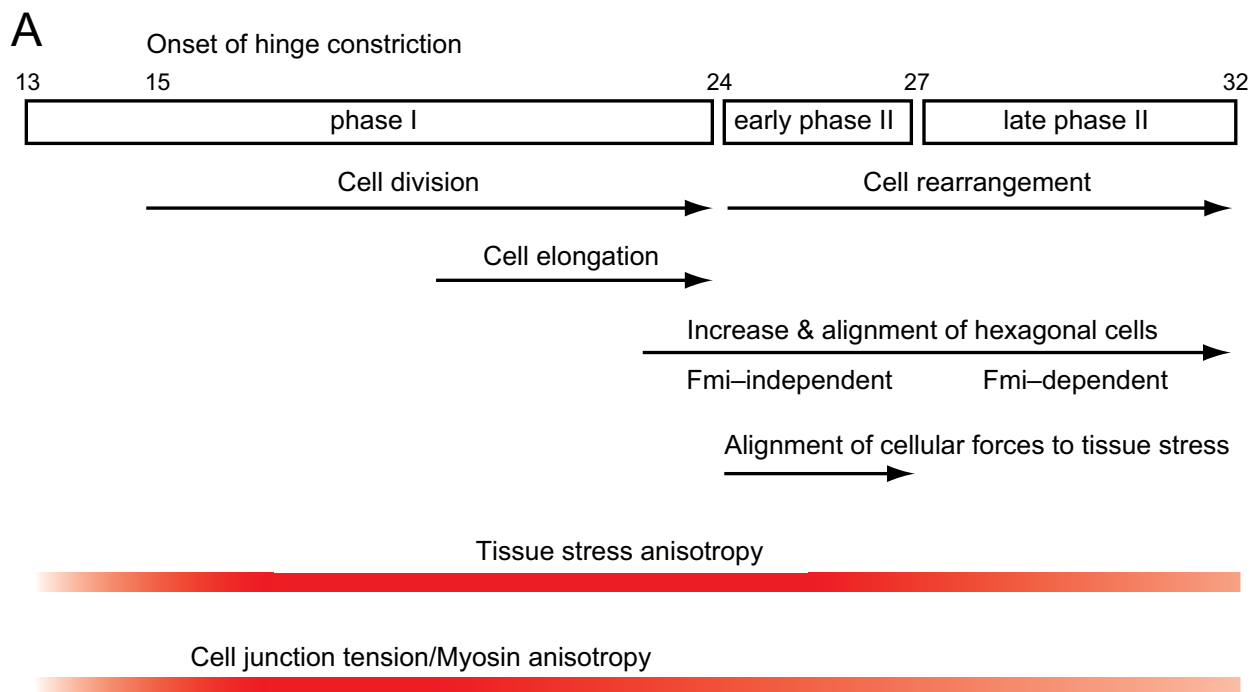

Fig. S11. In *flamingo* (*fmi*) RNAi wing, hexagonal packing proceeded normally until 27.5 h APF, but was disrupted afterwards.

A

Onset of hinge constriction

| 13 | 15 | | 24 | 27 | 32 |

phase I | early phase II | late phase II

Cell division →

Cell rearrangement →

Cell elongation →

Increase & alignment of hexagonal cells →

Fmi–independent   Fmi–dependent

Alignment of cellular forces to tissue stress →

Tissue stress anisotropy

Cell junction tension/Myosin anisotropy

B

**Tissue
(Cell–population)**

stress field
hexagonal packing

2
3

Cell

orientation of
hexagonal cells
junctional remodeling

1
4

Molecule

myosin

force–generating
force–responsive

Fig. S12. Summary of tissue mechanics and cell-level dynamics that underlie hexagonal cell packing.
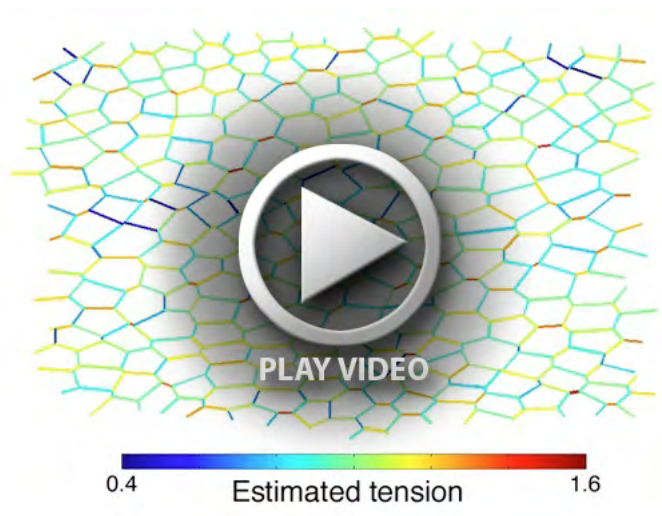
Movie 1. Ablation of a group of cells in the wing. A wing at 22 hours APF. Anterior is up and proximal is left. Cells at the center were ablated. The anisotropic extension of cell group contour confirmed the PD bias of global stress in the wing. Time label of the movie is: 14", -4", 4", 14", 24", … , 214" (laser irradiation was at 0 seconds). The fly genotype is *DEcadherin-GFP* knock-in. Scale bar: 20 μm.

Movie 2. Ablation of a group of cells in the scutum. A scutum at 22 hours APF. Anterior is left. Cells at the center were ablated. Note that the anisotropy in the outward velocity of cells was smaller in the scutum than in the wing (compare Movies 1 and 2). The time label of the movie and fly genotype are as described in the legend of Movie 1. Scale bar: 20 μm.

Movie 3. Temporal dynamics of the inferred tensions. Time-lapse images were taken from 23.5-30.5 hours APF, and data from 25-26 hours APF were extracted at 3-minute intervals. The arrowheads and arrows point to the AP and PD edges, respectively. The fly genotype is as described in the legend of Fig. 1.

Appendix 1 by Sugimura and Ishihara.

§1. Force-inference method

1-A Force inference of pressures and tensions

The algorithm for inferring mechanical forces in a tissue was reported by Ishihara and Sugimura, 2012. In the method, an input is a segmented image of epithelial tissue represented by polygonal tile. Deviations from 120° angles between cell contact surfaces indicate heterogeneities in tensions and pressures, which can be found by solving a linear inverse problem (it is underdetermined, but can be solved under reasonable physical assumptions such as positivity of cell junction tensions). The difference of pressures among cells (ΔP_i) and tensions along cell contact surfaces (T_{ij}) are inferred up to a scaling factor; the estimated tensions and pressures are related to true ones as $\Delta P_i = cP_i^{true} + P_0$ and $T_{ij} = cT_{ij}^{true}$, where c is a scaling factor and P_0 is the baseline value of the pressure. P_0 is set so that the sum of ΔP_i is zero. Scaling factor c is set to satisfy that the average of estimated tensions is unity. In the developmental stages analyzed in this study, the average V_{max} of the vertices after cutting single cell contact surface did not change extensively; the average V_{max} was 0.153 ± 0.054 μm/sec at 25.5–27.5 h APF (n = 21) and 0.132 ± 0.044 μm/sec at 30–32 h APF (n = 24) (Fig. S5D1, E1).

1-B Global tissue stress and local cell stress

Global (tissue) stress tensor **N** is given by the following matrix that integrates all cell pressures and tensions (see Fig. 1E for schematic representations) (Batchelor, 1970; Ishihara and Sugimura, 2012).

$$N_{\mu v} = \left[-\sum_{i:cell} A_i P_i \delta_{\mu v} + \sum_{\langle ij \rangle:edge} T_{ij} \frac{l_{ij}^{\mu} l_{ij}^{v}}{\left\| l_{ij} \right\|} \right] \Big/ \sum_{i:cell} A_i$$

Here, (μ,v) are indices for (x,y) and $\delta_{\mu v}$ is Kronecker's delta. A_i is the area of the ith cell in the plane of the adherens junction, and $\boldsymbol{l}_{ij} = (l_{ij}^{x}, l_i^{yv})$ is a vector representation of the edge shared by the ith and jth cell. The global stress tensor is symmetric and thus is represented as a stress ellipse (insets in Figs. 2A3–C3, 4A3–C3).

We defined the local cell stress tensor by $N_{\mu\nu}{}^i = (-\Delta P_i A_i \delta_{\mu\nu} + \Sigma_j T_{ij} l_{ij}{}^\mu l_{ij}{}^\nu / \|l_{ij}\|)/A_i$ for individual cells (Ishihara and Sugimura, 2012) (see Fig. 1E for schematic representations). i is the index of the cell, A_i and ΔP_i are the area and the estimated relative value of the cell pressure, respectively, and T_{ij} is the estimated tension of cell contact surface between the ith and neighboring jth cell. Vector $\mathbf{l}_{ij} = (l_{ij}{}^x, l_{ij}{}^y)$ represents the relative position of two endpoints of the cell contact surface, and $\|l_{ij}\|$ is its length. μ and ν are indices of x and y. Σ_j represents taking the summation on the cell contact surfaces between the ith and adjacent cells. The obtained tensors are represented by cross symbols for respective cells. Anisotropy of local stress is measured by $a - b$ or a/b, where a and b are eigenvalues of the local cell stress tensor. The direction of global stretch is obtained by the eigenvector of the global stress tensor. Local cell stress along the global stress direction of the tissue is measured from the local cell stress tensors and the direction of global stretch.

§2. Numerical simulation

2-A Implementation of numerical model

Here we describe details of implementations of the numerical simulations. To simulate rearrangement of cells, we employed a vertex model with the following form for potential energy (Honda, 1983; Graner and Sawada, 1993; Ouchi et al., 2003; Mofrad and Kamm, 2006; Farhadifar et al., 2007; Käfer et al., 2007; Lecuit and Lenne, 2007; Rauzi et al., 2008):

$$U\left(\{\mathbf{x}_i\}, \lambda_x, \lambda_y\right) = U_0\left(\{\mathbf{x}_i\}\right) - \lambda_x T_x(t) - \lambda_y T_y(t), \qquad \text{(eq. S2-1)}$$

$$U_0\left(\{\mathbf{x}_i\}\right) = \sum_{i:\text{cell}} U_{ar}(A_i) + \sum_{[ij]:\text{edge}} U_{lin}(l_{ij}) + \sum_{i:\text{cell}} U_{cor}(L_i). \qquad \text{(eq. S2-2)}$$

A_i and L_i represent the area and peripheral length of the ith cell at the plane of the adherens junction, respectively. l_{ij} is the length of the contact surface between the ith and jth cells. A_i, L_i, and l_{ij} are determined by positions of the vertices $\{\mathbf{x}_i\}$ which define the geometry of cells. In eq. S2-2, the first term represents the area elasticity of a cell and is given by $U_{ar}(A) = (K/2)(A - A_0)^2$. The second term $U_{lin}(l) = \sigma l$ represents line tension (sum of cell adhesion and contracting force), and the third term $U_{cor}(L) =$

$(\Lambda/2)L^2$ represents cortical elasticity (Fig. S8A). In eq. S2-1, tissue stretch is introduced with the last 2 terms (Andersen, 1980; Frenkel and Smit, 2001), where λ_x and λ_y are new variables for parameterizing the system size as $L_x = \lambda_x L^0_x$ and $L_y = \lambda_y L^0_y$. $T_x(t)$ and $T_y(t)$ are applied stresses along the x- and y-axes, respectively. The ordinary differential equations to be solved are derived as follows.

$$\begin{cases} \dfrac{dx_i}{dt} = -\lambda_x^2 F_i^x + \dfrac{T_x - \hat{T}_{xx}}{\lambda_x} x_i \\[2mm] \dfrac{dy_i}{dt} = -\lambda_y^2 F_i^y + \dfrac{T_y - \hat{T}_{yy}}{\lambda_y} y_i \\[2mm] \dfrac{d\lambda_x}{dt} = T_x - \hat{T}_{xx} \\[2mm] \dfrac{d\lambda_y}{dt} = T_y - \hat{T}_{yy} \end{cases} \qquad \text{(eq. S2-3)}$$

Here, $\mathbf{F}$ is given by $-\partial U_0/\partial \mathbf{X}$ and $\hat{\mathbf{T}}$ is given by the following equation.

$$\hat{T}_{\mu\nu} = \sum_{i:cell} K(A_i - A_0)A_i + \sum_{[ij]:edge} \left(\sigma_{ij} + \Lambda(L_i + L_j) \right) \frac{l_{ij}^\mu l_{ij}^\nu}{\left\| \mathbf{l}_{ij} \right\|} \qquad \text{(eq. S2-4)}$$

With these equations $dU/dt \leq 0$ is assured when $\mathbf{T}(t) = (T_x(t), T_y(t))$ is constant. In the final steady state, $\mathbf{F}_i = 0$ for all i and $\mathbf{T} = \hat{\mathbf{T}}$ were satisfied as expected. In this implementation, introduced variables λ_x and λ_y that involve the global geometry of the system have no intuitive physical interpretation, but this methodology is widely used due to their technical advantages for simulating the dynamics under the specified stress environment with the periodic boundary condition (Frenkel and Smit, 2001).

In addition, fluctuation is included into the simulations so that the system is not trapped in a local minimum. One of the convenient ways is to add noise terms to line tension in the following form:

$$\dot{\sigma}_{ij} = -\tau^{-1} \left(\sigma_{ij} - \sigma_0 \right) + z\sigma_0 \sqrt{2/\tau} \xi_{ij}(t) \qquad \text{(eq. S2-5)}$$

Here, $\xi_{ij}(t)$ represents white Gaussian noise with $\langle \xi_{ij}(t) \rangle = 0$ and $\langle \xi_{ij}(t)\xi_{kl}(t') \rangle = \delta_{ij,kl}\delta(t - t')$. σ_{ij} fluctuates around its average σ_0. τ determines the time scale of the fluctuation, and z controls its magnitude as $z = \langle |\sigma_{ij} - \sigma_0| \rangle / \sigma_0$.

The stochastic differential equations were numerically solved where junctional remodeling (T1 process) was allowed. To simulate the process of cell rearrangement without an extrinsic force (Fig. 3H, upper left), both $T_x(t)$ and $T_y(t)$ were set to 0.10 (an offset value) for all t. For the isotropic stretch (Fig. 3H, upper right), both $T_x(t)$ and $T_y(t)$ were set to 0.10 for $0 < t < 50.0$, and then were increased rapidly according to $T_x(t) = T_y(t) = 0.10 + 0.05 \times (t - 50.0)$ until they reached $T_x(t) = T_y(t) = 0.20$ at $t = 70.0$, and were constant afterward. For the anisotropic stretch along the x-axis (Fig. 3H, below), $T_y(t) = 0.10$ for all t and $T_x(t)$ was set as for the isotropic stretch condition.

Among the parameters of the potential U_0, the values of K and A_0 are arbitrary by choosing the proper scales for physical dimensions (length and force); they were set as $K = 100.0$ and $A_0 = 1.0/256.0$ for this study. In the model, as the derivative of U_{cor} with respect to l shows, the coefficient of the quadratic term Λ is responsible for the length dependence of the tension at an edge. We found that Λ should be finite positive to reproduce the experimentally observed negative correlation between tensile force and edge length in the numerical simulations (Rauzi et al., 2008). In Figs. 3H, I, S8, we set σ_0 and Λ to $\tilde{\sigma}_0 = \sigma_0 / K A_0^{3/2} = 0.12$ and $\tilde{\Lambda} = \Lambda / K A_0 = 0.04$, as previously reported for the *Drosophila* wing disc, to reproduce the observed distribution of n-sided polygons and their areas after cell division (Farhadifar et al., 2007). Using these values, edge length and tension had a reasonable negative correlation.

Eventual fractions of hexagonal cells were nearly same for the 3 conditions at large and slow noise ($z = 50\%$ and $\tau^{-1} = 0.1$ in Fig. S8C). However, in most of the parameter regions examined, the eventual fraction of hexagonal cells under horizontal stretch was significantly larger than that under isotropic stretch (Figs. 3H–J, S8B). In addition, parameter dependence on τ differed among the 3 conditions; with large z, the fraction of hexagonal cells under no or isotropic stretch depended on τ (squares and crosses in Fig. S8C), whereas that under horizontal stretch did not (circles in Fig. S8C).

2-B Changes in cell shapes

Deformation of a tissue consists of a change in the shapes of constitutive cells and/or cell-cell intercalations (Blanchard et al., 2009). At an early phase of the simulations, application of isotropic or horizontal stretch triggered expansion or directional elongation of the cells, respectively (see $t = 50–250$ in Fig. 3H, upper right and below). Under an isotropic stretch, expansion of the cells reached a plateau due to their area elasticity, while cell intercalation among the cells was not biased and newly formed cell-cell surfaces were distributed isotropically (Fig. S8D). Therefore, the shape of the entire tissue changed only slightly between $t = 250$ and 2000 (Fig. 3H, upper right). On the other hand, under a horizontal stretch, biased cell intercalation caused formation of new cell-cell surfaces in the horizontal direction (Fig. S8E). Elongation of the constituent cells after $t = 250$ was not evident; hence, the biased intercalations were responsible for horizontal elongation of the tissue at this phase (see $t = 250–2000$ in Fig. 3H, below).

2-C Numerical Simulation with biased tensile parameter

Numerical model with biased tensile parameter was simulated as follows (Fig. 6A2). The model is obtained by replacing the line tension parameter σ in (eq. S2-2) by $\sigma (1 – \mu\cos2\theta)$, where μ represents the magnitude of anisotropy. θ is the direction of the cell contact surface, thus the vertical contact surfaces in the figure have larger tension than horizontal ones. The system was under the isotropic pressure environment and we set $T_x = T_y = 0.10$. Λ and μ are controlled to obtain the results shown in Fig. 6B–D. The other parameters are set the as same as those described in §2-A.

In both tissue stretch and biased tensile parameter models, the anisotropy of cell shape (R_T) correlated less with the fraction of hexagonal cells than the orientation of cell contact surface ($\langle\cos6\theta_j\rangle$) did (Fig. 6B–D). Therefore, although wing cells are elongated along the PD axis by the hinge constriction before reordering cell packing (~24 h APF) (Fig. 2A1, 2D2), it is suggested that cell elongation affects hexagonal cell packing less significantly than alignment of hexagonal cells.

5

Supplemental References

Andersen, H. C. (1980). Molecular-Dynamics Simulations at Constant Pressure and-or Temperature. *Journal of Chemical Physics* **72**, 2384-93.

Blanchard, G. B., Kabla, A. J., Schultz, N. L., Butler, L. C., Sanson, B., Gorfinkiel, N., Mahadevan, L. and Adams, R. J. (2009). Tissue tectonics: morphogenetic strain rates, cell shape change and intercalation. *Nat Methods* **6**, 458-64.

Frenkel, D. and Smit, B. (2001). Understanding molecular simulation: From Algorithms to Applications, San Diego: Academic press.

Gubb, D., Green, C., Huen, D., Coulson, D., Johnson, G., Tree, D., Collier, S. and Roote, J. (1999). The balance between isoforms of the prickle LIM domain protein is critical for planar polarity in Drosophila imaginal discs. *Genes Dev* **13**, 2315-27.

Ma, D., Yang, C. H., McNeill, H., Simon, M. A. and Axelrod, J. D. (2003). Fidelity in planar cell polarity signalling. *Nature* **421**, 543-7.

Matakatsu, H. and Blair, S. S. (2004). Interactions between Fat and Dachsous and the regulation of planar cell polarity in the Drosophila wing. *Development* **131**, 3785-94.